Remote Sensing of Environment 346 (2026) 115614

Contents lists available at ScienceDirect

Remote Sensing of Environment

journal homepage: www.elsevier.com/locate/rse

The cmSCOPE-D model: A transmission-dynamics-enabled SCOPE adaptation to characterize vertically stratified heterogeneity of maize disease stress

Binxiang Qian [a,b,c,d], Wenjiang Huang [a,b,*], Zhijun Zhen [e], Kehui Ren [a,b], Peiqi Yang [f], Jianbo Qi [g], Michael Henke [h], Xiuliang Jin [i], Lingjing Ouyang [g], Anting Guo [a,b], Jie Bai [j], Chao Ruan [k], Tiecheng Huang [l], Yin Jin [a,b], Zhenong Jin [c,d,*]

[a] State Key Laboratory of Remote Sensing Science, Aerospace Information Research Institute, Chinese Academy of Sciences, Beijing, China
[b] University of Chinese Academy of Sciences, Beijing, China
[c] Institute of Ecology, College of Urban and Environmental Science, Peking University, Beijing, China
[d] State Key Laboratory for Vegetation Structure, Function and Construction (VegLab), Peking University, Beijing, China
[e] Centre d'Etudes Spatiales de la Biosphère (CESBIO), Université de Toulouse, University of Toulouse 3 (UT3)-Paul Sabatier/National Centre for Space Studies (CNES)/National Center for Scientific Research (CNRS)/National Institute of Agricultural Research (INRAE)/Research Institute for Development (IRD), Toulouse, France
[f] School of Geography, Nanjing Normal University, Nanjing, China
[g] Advanced Interdisciplinary Institute of Satellite Applications, Beijing Normal University, Beijing, China
[h] Innovation Platform for Seed Design, Yazhouwan National Laboratory, Sanya, China
[i] Crop Phenotypic Innovation Research Group, Institute of Crop Science, Chinese Academy of Agriculture Sciences, Beijing, China
[j] School of Resources and Environment, University of Electronic Science and Technology of China, Chengdu, China
[k] National Engineering Research Center for Agro-Ecological Big Data Analysis and Application, Anhui University, Hefei, China
[l] College of Forestry and Landscape Architecture, Xinjiang Agricultural University, Xinjiang, China

ARTICLE INFO

Editor: Jing M. Chen

Keywords:
Coupled maize model
mSCOPE model
SEIR model
3D lesion distribution
Disease stress traits
Radiative transfer model

ABSTRACT

Accurate monitoring of maize diseases is crucial for global food security, yet current remote sensing approaches lack mechanistic quantification of disease development. To address this issue, we proposed a disease transmission dynamics module of the cmSCOPE-D (**c**oupled **m**aize - m**SCOPE**) model by integrating epidemic dynamics with canopy radiative transfer theory, enabling full-process simulation from pathogen infection to canopy optical responses. The proposed module offers advancements in three key areas: 1. Extending the Susceptible-Exposed-Infectious-Removed (SEIR) model into a maize disease transmission dynamics module with environmental response functions, systematically quantifying the effects of temperature, humidity, and growth stage; 2. Establishing dynamic equations for leaf biochemical components as functions of the Disease Index (DI); 3. Formulating rules for 3D lesion spatial distribution that follow natural infection patterns.

Our module was validated using field data, with relative errors in DI simulation below 3% and high retrieval accuracy for key biochemical components (chlorophyll and carotenoids; NRMSE <0.2). Our results revealed two key findings: First, the three-dimensional spatial distribution of lesions and disease severity were critical factors driving the canopy spectral signature, with the strongest modulation on reflectance originating from middle-canopy lesions due to their larger projected proportion in the viewing direction. Second, under disease stress, solar-induced chlorophyll fluorescence (SIF) exhibited decreased intensity and a blue-shifted peak, while the reflectance spectrum showed a blue shift in the red-edge position. These findings provide a new theoretical basis for early disease detection. We also identified that current leaf-level radiative transfer models do not adequately represent disease-specific physicochemical changes, highlighting a priority for future model refinement. Overall, the proposed module offers theoretical and methodological advancement for crop disease remote sensing, as it enhances understanding of optical response mechanisms under disease stress and establishes a foundation for intelligent monitoring and early-warning systems.

* Corresponding authors.
E-mail addresses: huangwj@aircas.ac.cn (W. Huang), jinzhenong@pku.edu.cn (Z. Jin).

https://doi.org/10.1016/j.rse.2026.115614
Received 15 October 2025; Received in revised form 12 April 2026; Accepted 8 August 2026
Available online 18 August 2026
0034-4257/© 2026 Elsevier Inc. All rights are reserved, including those for text and data mining, AI training, and similar technologies.

1. Introduction

Maize is vital for global food security, serving as a key source of food, feed, and bioenergy. However, the increasing frequency and severity of maize diseases, exacerbated by intensive cultivation practices and climate change, pose a significant threat to yield and grain quality (Pfordt and Paulus, 2024; Shen et al., 2024). This leads to substantial losses, including a 10.4% global mean yield loss from fungal pathogens (Savary et al., 2019).

Traditional monitoring through manual field surveys is subjective, labor-intensive, and spatially limited, making it inadequate for large-scale precision agriculture. Remote sensing offers a promising alternative with its capabilities for non-destructive, cost-effective, and spatially continuous assessment (Mahlein, 2016; Zhang et al., 2019). Disease stress induces alterations in crop physiology and biochemistry, leading to detectable changes in canopy spectral features, including shifts in visible and near-infrared reflectance and abnormal responses in solar-induced chlorophyll fluorescence (SIF), which is directly linked to photosynthetic function (Zhang et al., 2019).

Common foliar fungal diseases, such as Maize CurvuLaria Leaf Spot (MCLLS), Maize Southern Leaf Blight (MSLB), Maize Northern Leaf Blight (MNLB), and Maize Southern Rust (MSR) (Pfordt and Paulus, 2024), influence optical responses through processes at multiple scales. At the biochemical level, infection disrupts chloroplasts, impairs photosynthesis and respiration, and substantially reduces chlorophyll (C_{ab}), carotenoids (C_{ar}), equivalent water thickness (C_w), and dry matter content (C_{dm}) (Bai et al., 2024; Jing et al., 2022; Zhang et al., 2019). At the leaf structural level, lesion formation and necrosis alter cellular integrity, creating vertical heterogeneity within canopies (typically concentrated in middle and lower layers) that directly affects spectral detectability (Cao et al., 2013; Zhang et al., 2019). At the canopy structural level, disease-induced leaf desiccation and biomass loss reduce the leaf area index (LAI) and modify leaf angle distribution (Liu et al., 2023). These biochemical and structural alterations lead to predictable changes in leaf optical properties. Chlorophyll degradation increases visible reflectance, lesion formation enhances near-infrared scattering, and reduced water and dry matter content elevate shortwave infrared reflectance (Bai and Jin, 2024; Bai et al., 2025; Liu et al., 2023). Characterizing these spectral responses across disease severity levels is therefore essential for remote sensing-based diagnosis and early detection of maize diseases (Guo et al., 2024; Luo et al., 2021; Lv et al., 2023).

Nevertheless, diagnosing diseases based solely on spectral signals remains challenging. Empirical or index-based methods face critical limitations: (1) susceptibility to domain shift across locations, cultivars, and management practices, as model performance is highly sensitive to variations in these background conditions (Tian et al., 2021); (2) spectral confounding with other stresses like nutrient or water deficiency, since these stresses induce overlapping spectral responses (Gao et al., 2020; Zhang et al., 2012); and (3) lack of dynamic transferability to evolving disease stages, as models calibrated for a specific time point or symptom stage often fail at other phases of disease progression (Mahlein et al., 2013). It is widely recognized that addressing these challenges necessitates the development of mechanistic models (Bai et al., 2025). This diagnostic uncertainty underscores the urgent need for mechanistic remote sensing models grounded in epidemiological dynamics to enable robust and accurate monitoring.

Substantial progress has been made in mechanistic disease modeling by considering host-pathogen-environment interactions. The Susceptible-Exposed-Infectious-Removed (SEIR) model has been widely adapted to simulate crop disease dynamics due to its flexibility (Cunniffe et al., 2012; El Jarroudi et al., 2025; Soubeyrand et al., 2008). For instance, Aloyce et al. developed an SI-SEI structured model for Maize Lethal Necrosis disease (Aloyce et al., 2017), with subsequent refinements incorporating environmental response functions to capture seasonal climatic impacts on spread (Kapange et al., 2019) and integrating crop phenological stages as key determinants of disease dynamics (Xiao et al., 2022). These advances provide a crucial theoretical foundation for simulating diseases spatiotemporal progression linked to remote sensing observations.

Radiative transfer models (RTMs) are essential tools for interpreting remote sensing signals from heterogeneous canopies. 1D heterogeneous RTMs, such as the two-layer ACRM (Kuusk, 2001), multi-layer MRTM (Wang and Li, 2013) and the multi-layer mSCOPE model (Yang et al., 2021; Yang et al., 2017), approximate vertical heterogeneity by stacking horizontal layers with distinct optical properties. In addition, stochastic radiative transfer theories (Li et al., 2020; Li et al., 2022; Shabanov et al., 2000) provide a statistical framework to account for spatial heterogeneity (both vertical and horizontal) in canopy structure and physiology, using moments such as the probability of finding foliage elements and pair-correlation functions. More sophisticated 3D RTMs, including radiosity-based (e.g., RAPID (Huang et al., 2013)) and ray-tracing-based models (e.g., DART (Gastellu-Etchegorry et al., 1996), LESS (Qi et al., 2017; Qi et al., 2019)), explicitly simulate internal radiation transport, offering a powerful tool for investigating complex disease patterns. Recent studies have leveraged these models to analyze the impact of heterogeneously distributed damaged foliage on fluorescence signals (Li et al., 2020; Li et al., 2022) and to evaluate the potential of advanced sensors for disease detection (Zhang et al., 2025; Zhao et al., 2023).

However, existing research on disease detection using remote sensing is largely static, failing to dynamically couple epidemiological models with the 3D canopy scenes in RTMs. Consequently, how vertical canopy heterogeneity evolves with disease progression to affect optical and SIF signals is poorly understood. This paper is the second in a two-paper series on the cmSCOPE framework. The companion paper (Qian et al., 2026) introduced the core cmSCOPE model and demonstrated that vertical heterogeneity in canopy structure—particularly leaf inclination angle—exerts a dominant influence on canopy reflectance and solar-induced fluorescence. Building on this framework, the present study integrates a disease transmission dynamics module based on the Susceptible-Exposed-Infectious-Removed (SEIR) model and develops an extended model, cmSCOPE-D. The two primary contributions of this model are: (1) coupling SEIR epidemiological dynamics with canopy radiative transfer to enable end-to-end simulation from pathogen infection to canopy optical responses; and (2) developing a dynamic disease scene generator that explicitly represents the three-dimensional spatial distribution of lesions and the dynamic responses of leaf biochemical components to disease progression, thereby systematically capturing the spatiotemporal evolution of canopy structure and optical properties under disease stress. While the original cmSCOPE focused on the role of canopy structural heterogeneity under growth and abiotic stress, cmSCOPE-D establishes a mechanistic link between disease epidemiology and canopy optical properties.

Model performance was examined through a comprehensive evaluation scheme covering key processes including disease dynamics, retrieval of leaf biochemical parameters, and multi-scale optical signal simulation, with comparative analysis against field measurements and physical model simulations. Our overarching goal is to establish an end-to-end simulation framework that links disease transmission, physiological response, signal generation, and accuracy assessment. This framework provides a novel model-based tool and strengthens the mechanistic understanding of remote sensing applications for maize disease detection.

2. Materials and methods

2.1. Research framework

Fig. 1 depicts the technical workflow of this study, comprising four key components: **(1) Data acquisition:** Collection of multi-source data, including leaf biochemical components, hyperspectral reflectance, canopy structural parameters, meteorological station data, and field-

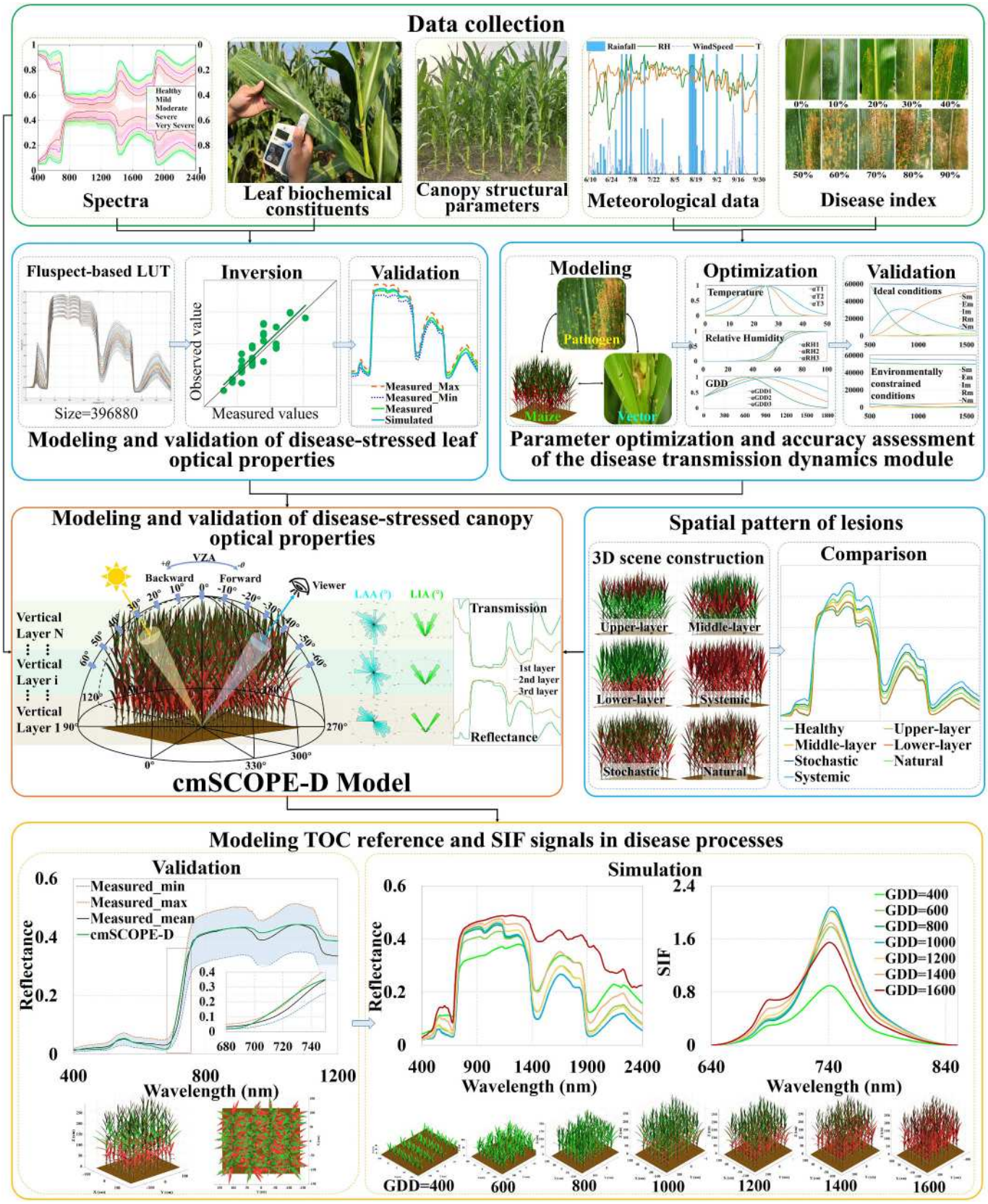


Fig. 1. Technical workflow of this study. The figure illustrates the four core components of this study: data acquisition (green box), model development (blue box) and integration (orange box), model validation (yellow box), and signal analysis (yellow box). (For interpretation of the references to colour in this figure legend, the reader is referred to the web version of this article.)

surveyed DIs, to construct realistic canopy scenarios under disease stress; **(2) Model development and integration:** Construction of a leaf optical properties look-up table (LUT) using the Fluspect-B model (Vilfan et al., 2016) for biochemical component retrieval; optimization of SEIR model parameters to simulate disease transmission dynamics; and establishment of multiple spatial lesion distribution patterns to characterize canopy heterogeneity. These components were integrated into the cmSCOPE-D model to simulate canopy reflectance and SIF under varying disease conditions; **(3) Model validation:** Evaluation of individual modules and the integrated model performance by

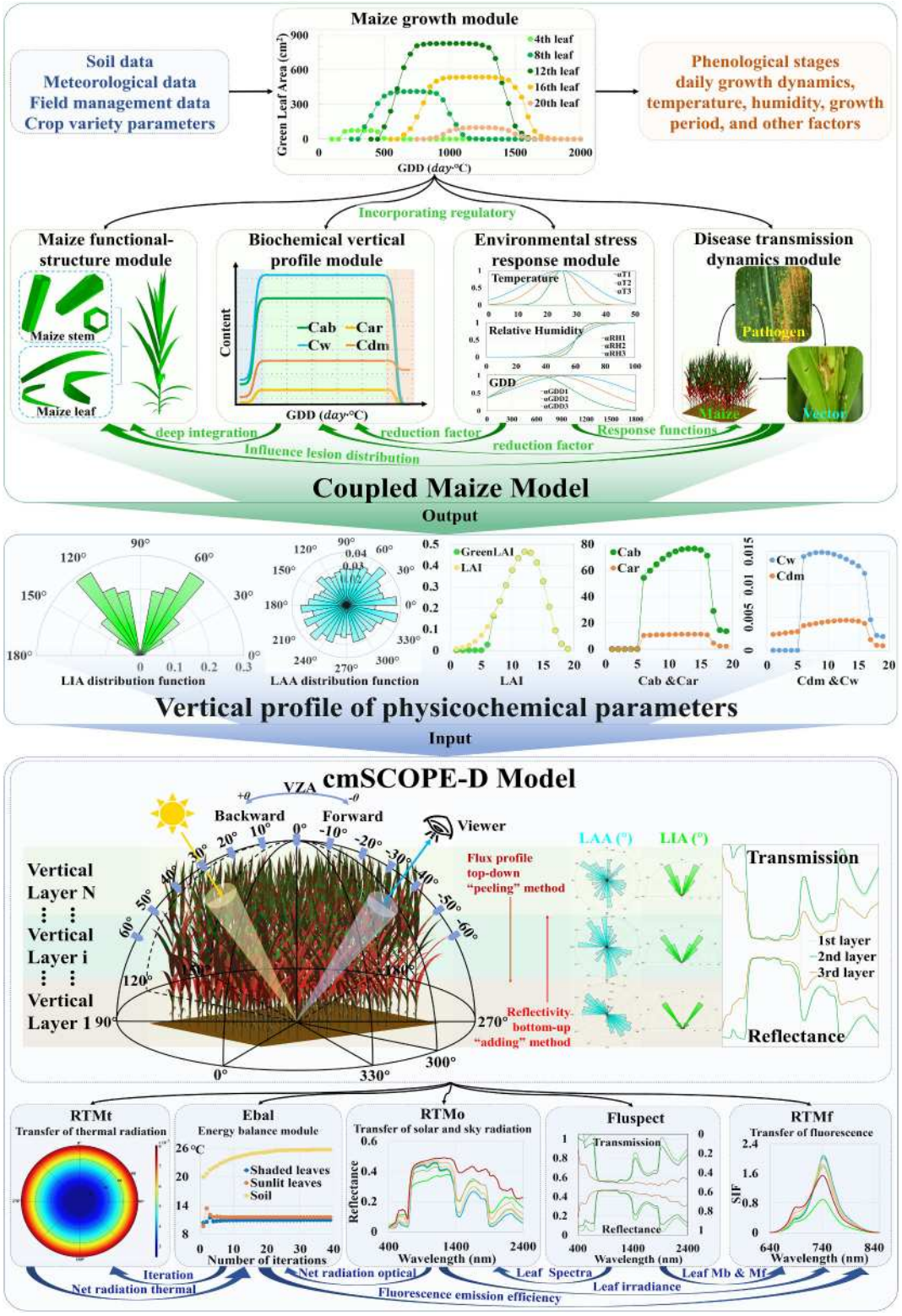


Fig. 2. Schematic diagram of the cmSCOPE-D model architecture. The figure shows three vertically arranged panels. The upper panel represents the Coupled Maize model, which generates vertical profiles of canopy physicochemical parameters (middle panel) as inputs to the mSCOPE model (lower panel). Arrows indicate the direction of parameter transfer. The integrated architecture enables end-to-end simulation from maize growth drivers to canopy optical signals.

comparing simulated and measured leaf reflectance, canopy reflectance, and DI under disease stress; **(4) Signal analysis:** Systematic investigation of canopy reflectance and SIF under disease stress, emphasizing red-edge position and SIF peak bands for disease severity monitoring and early detection.

2.2. Description of cmSCOPE-D model

2.2.1. Overview of the cmSCOPE-D model

As shown in Fig. 2, the cmSCOPE-D model integrates a disease transmission dynamics module (**Section 2.2.2**) on top of the cmSCOPE framework (Qian et al., 2026). The Coupled Maize model (the upper panel) simulates growth dynamics and stress responses through five modules: thermal-time-driven growth, canopy functional-structural modeling, environmental stress response, disease transmission dynamics, and biochemical vertical profiling. It outputs vertical profiles of canopy physicochemical parameters (the middle panel) as inputs to the mSCOPE model (the lower panel). The mSCOPE model, derived from the original SCOPE model, simulates canopy optical and energy balance processes via Fluspect-B (leaf-scale biochemistry), the canopy-scale radiative transfer modules (RTMo for optics, RTMf for fluorescence, and RTMt for thermal), and Ebal (energy balance). This integrated architecture enables end-to-end simulation from maize growth drivers to canopy optical signals, and is extended in this study to account for disease stress.

2.2.2. Disease transmission dynamics module

To dynamically simulate and mechanistically interpret maize canopy reflectance and SIF under disease stress, we developed a disease transmission dynamics module within the cmSCOPE framework (Qian et al., 2026). Based on host-vector-pathogen interactions and extending the classic SEIR model, this module uses environmental drivers like temperature, relative humidity, and GDD to simulate the spatiotemporal progression of pathogens. Through bidirectional coupling with the canopy functional-structural and biochemical profile modules, it achieves end-to-end simulation from pathogen infection to canopy optical responses, outputting the population-level DI, 3D lesion distribution, and dynamic trends in key biochemical components. The systematic construction of this module encompasses three core components:

(1) SEIR model Formulation. The SEIR framework encompasses maize host populations, vector populations, and pathogen populations (P_o). Maize hosts are divided into four subpopulations: susceptible (S_m), exposed (E_m), infectious (I_m), and removed (R_m). Vector populations comprise susceptible (S_v), infectious (I_v), and removed (R_v) subpopulations. The core transmission pathway involves susceptible maize (S_m) transitioning to the exposed state (E_m) at rate η under the combined influence of environmental pathogens (P_o), infectious maize (I_m), and infectious vectors (I_v). Exposed individuals progress to the infectious state (I_m) at rate α_m, then to the removed state (R_m) at mortality rate σ_m. Susceptible vectors (S_v) are recruited at rate Λ, experience natural mortality at rate μ_v, and transition to the infectious state (I_v) at rate $\lambda(P_o, I_m)$. Pathogen dynamics are governed by release from infectious maize

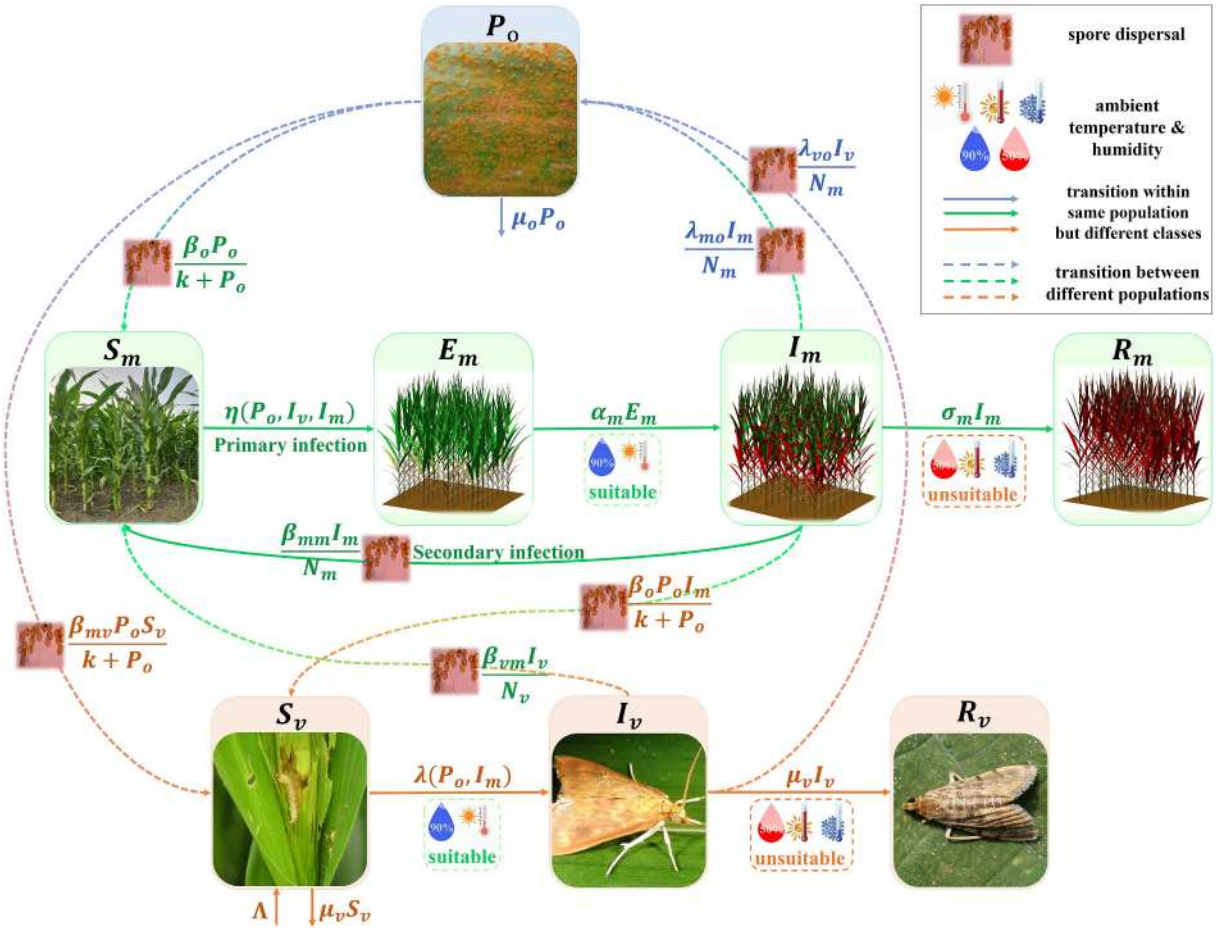


Fig. 3. Schematic of the SEIR model integrated with host-vector populations. The model divides maize hosts into susceptible (S_m), exposed (E_m), infectious (I_m), and removed (R_m); vectors into susceptible (S_v), infectious (I_v), and removed (R_v); and includes environmental pathogens (P_o). Solid arrows indicate internal state transitions; dashed arrows represent cross-population interactions. Specifically, η, infection rate of S_m; Λ, recruitment rate of S_v; α_m, progression rate from E_m to I_m; σ_m, disease-induced mortality rate of I_m; μ_o, decay rate of P_o; μ_v, natural mortality rate of vectors; λ_{mo} and λ_{vo}, pathogen release rates from I_m and I_v; k, carrying capacity per plant for vectors; β_o and β_{ov}, contact rates of environmental pathogens with S_m and S_v; β_{mv} and β_{mm}, transmission rates from I_m to S_v and S_m.

and vectors (at rates λ_{mo} and λ_{vo}) and natural decay (at rate μ_o). Fig. 3 illustrates these multi-population interactions, where solid arrows indicate internal state transitions and dashed arrows represent cross-population interactions. The model's five fundamental assumptions and complete differential equation system (**Eqs. A1a-A1k**) are provided in Appendix A1.1. A complete list of all model parameters is provided in Appendix **Table A5**.

(2) Environmental Response Functions for Transmission Parameters. Contact rates between populations (λ_{v_o}, λ_{m_o}) and transition rates within species (β_o, β_{ov}, β_{mv}, β_{mm}) are critical parameters governing disease transmission. These rates exhibit strong dependence on environmental factors (i.e., temperature, relative humidity, and crop growth stage) with optimal conditions varying across disease phases and populations. To quantitatively capture these environmental influences, we introduced temperature (α_T), relative humidity (α_{RH}), and phenological (α_{GDD}) response functions that dynamically adjust key transmission parameters. The specific mathematical formulations (Eqs. A2a-A2c), biological rationale for parameterization (**Table A 1**), and response curves across environmental gradients (**Fig. A 1**) are detailed in Appendix A1.2. In this study, simulation scenarios that incorporate these environmental response functions (α_T, α_{RH}, α_{GDD}) are referred to as environmentally constrained conditions, in contrast to ideal conditions where such environmental regulations are ignored.

(3) Disease Severity Quantification and Lesion Visualization. To translate population-level infection dynamics from the SEIR model into quantifiable disease severity and spatial lesion patterns, we established a hierarchical framework that: (i) implements a sigmoidal growth model relating individual plant disease severity to infection duration (**Fig. A 2**); (ii) calculates population-level DI by integrating daily new infections with the single-plant severity model; and (iii) defines spatial distribution rules mapping DI to lesion area proportions across canopy layers according to Chinese agricultural standard NY/T 3546–2020 (https://ndls.org.cn/standard/detail/47bbc34f601945576d2b8e16c250d434). These components are implemented through the Coupled Maize model's 3D triangular mesh to achieve dynamic lesion visualization. The mathematical models for severity calculation (**Eqs. A4a-A4c**), leaf grouping criteria (**Table A 2**), and disease rating mappings (**Table A 3**) are provided in Appendix A1.3.

2.2.3. Model parameterization

The cmSCOPE-D model operates by default with heterogeneous distribution patterns for leaf angle distribution (LAD; leaf inclination and azimuth) and sub-layer LAI (iLAI). Main model parameters are listed in Appendix **Table A 4**. The disease transmission dynamics module requires additional parameters (fundamental SEIR inputs and pathogen-specific parameters for the four maize diseases), detailed in Appendix **Table A 5**.

2.3. Study areas and data acquisition

2.3.1. Study areas

To develop and validate the disease transmission dynamics module of cmSCOPE-D model, field experiments were conducted in 2023 and 2024 across two representative summer maize production regions in China, targeting four major foliar diseases (i.e., MNLB, MCLLS, MSLB, and MSR). The first experiment was conducted on August 12–13, 2023, at the Tongzhou Experimental Station in Beijing (39°41.1′ N, 116°41.7′ E). Detailed descriptions of the site, including climate, soil properties, and experimental design, are provided in the companion paper (Qian et al., 2026). A total of 50 sampling plots (1 m × 1 m each) were established, comprising 26 healthy control plots and 24 diseased plots.

The second experiment was carried out from September 1–15, 2024, at the Xinxiang Comprehensive Experimental Base in Henan Province (35°8.5′ N, 113°47′ E). The site features a warm temperate continental monsoon climate with a mean annual temperature of 14.1 °C and mean annual precipitation of 548.3 mm, primarily concentrated in July–August. The experimental area elevation ranges from 70 to 82 m, with an annual sunshine duration of 2408 h. Favorable light and temperature conditions combined with suitable humidity during the maize growing season provided a typical environment for multiple foliar diseases (Bai et al., 2024). The mean cumulative GDD during the experiment was 1561 day·°C. The second experimental design consisted of 120 treatment plots (5.4 m × 3.6 m each), with 40 plots each assigned to healthy control, MCLLS inoculation, and MSLB inoculation treatments. Artificial inoculation was conducted in early August using an electric sprayer, while MSR infection occurred naturally. A total of 128 sampling points (1 m × 1 m each) were established across these plots, encompassing 40 healthy, 40 MCLLS-infected, 40 MSLB-infected, and 8 MSR-infected samples.

2.3.2. General data acquisition

Canopy structural parameters, leaf biochemical components, spectral data, and meteorological data were collected following the protocols described in the companion paper (Qian et al., 2026, Section 2.2). Key measurements included: **Canopy Structural Parameters**: LAI (LI-COR LAI-2200), plant height, leaf number, and leaf inclination angle (determined from plant photographs). **Biochemical Components**: C_{ab}, C_{ar}, C_w and C_{dm} determined via spectrophotometric and gravimetric methods. **Spectral Data**: Hyperspectral reflectance of canopy and components using an ASD FieldSpec® Pro FR spectroradiometer (350–2500 nm). **Disease Assessment**: Temperature, humidity, soil conditions, wind, and precipitation recorded at 10-min intervals using on-site monitoring systems (see **Fig. A 3** for complete records).

In addition to the above, this study includes three novel components specifically related to disease assessment, which are detailed in the following subsections.

2.3.3. Field survey of disease index

Field disease assessment followed the Chinese agricultural industry standard NY/T 3546–2020, which provides systematic guidelines for quantifying disease severity at the individual plant level and disease index at the population level.

Disease Index Calculation. The population-level DI was calculated using Eq. (1), which integrates severity distribution data from field surveys:

$$DI = \frac{\sum l_i \times d_i}{\sum L \times d_{max}} \times 100 \quad (1)$$

where d_i represents the disease severity level (on a scale from 0 to $d_{max} = 9$), l_i is the number of plants at that severity level, and L is the total number of plants investigated. Descriptions of disease severity levels for individual maize plants are provided in **Table A 3**.

Survey Implementation. In each 1 m × 1 m sampling plot, three maize plants were randomly selected, and the lesion proportion on each leaf was recorded to calculate individual plant disease severity. The plot-level DI was then derived using Eq. (1). Based on DI values, disease index was classified into five grades from Grade 1 (light) to Grade 5 (very severe), following the criteria in **Table A 3**. Field survey results of DI are shown in **Fig. A 4**.

Table 3 summarizes the directly measured biochemical components from leaf samples in each plot together with the corresponding plot-level DI. These measured data serve as a reference for validating the LUT-based inversion (Section 3.3.2).

2.3.4. Hyperspectral characteristics of diseased maize leaves

Based on field surveys, leaf samples were categorized into five severity levels: healthy (Grade 0), light (Grades 1–2), moderate (Grade 3), severe (Grade 4), and very severe (Grade 5). Fig. 4 illustrates the measured leaf spectral curves for each severity level across the four major foliar diseases (MCLLS, MSLB, MNLB, and MSR). Overall, as disease severity increases, leaf reflectance generally rises in the visible to

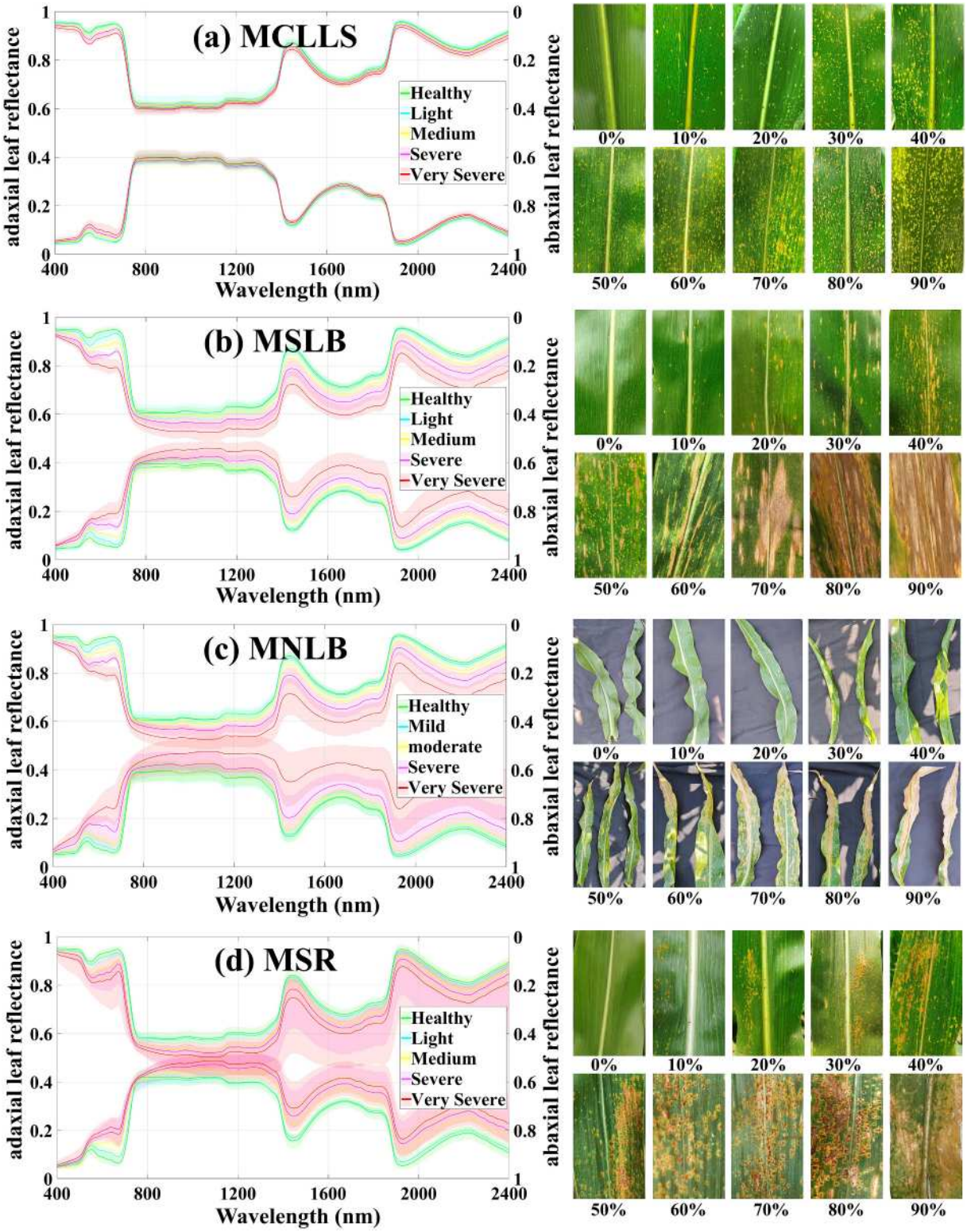


Fig. 4. Measured leaf spectral curves and corresponding maize leaf images under different disease severity levels. The figure shows leaf reflectance spectra (left) and photographs (right) for four maize diseases: (a) MCLLS, (b) MSLB, (c) MNLB, (d) MSR. Left: five severity levels (healthy to very severe). Right: ten lesion area classes (0%–90%).

red-edge region (~400–740 nm) and in the shortwave infrared region (~1300–2500 nm). However, in the near-infrared region (~740–1300 nm), light infected leaves exhibit lower reflectance than healthy leaves, whereas moderately to very severely infected leaves show higher reflectance. The leaf reflectance spectra for each severity level were averaged within each level. These averaged spectra were then used as input to the Fluspect-B model to retrieve leaf biochemical components (Cab, Car, Cw, Cdm) and the leaf structure parameter N via a look-up table (LUT) approach (see Section 2.4). The resulting regression equations relating these retrieved parameters to DI are presented in Table 4.

2.3.5. Spatial distribution patterns of canopy lesions

The spatial distribution of lesions within the canopy critically influences TOC reflectance and SIF (Zhao et al., 2023). Six representative distribution patterns were defined: upper-layer, middle-layer, and lower-layer infection, stochastic infection, natural infection, and systemic infection, with disease severity classified into four levels (light, moderate, severe, and very severe) based on DI. The six patterns serve distinct purposes: upper/middle/lower infections isolate the

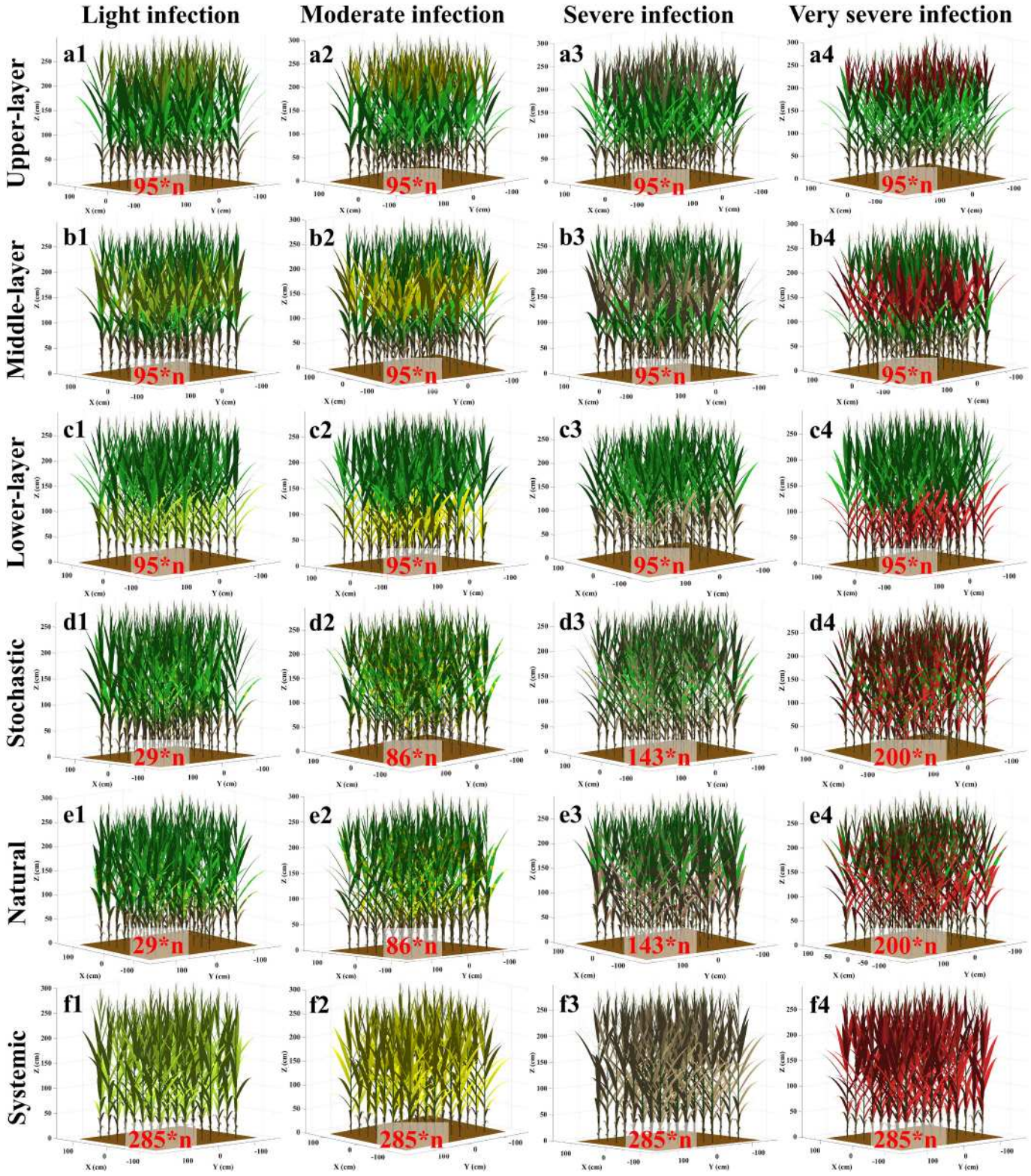


Fig. 5. Side views of maize canopies under different lesion distribution patterns and disease severity levels: (a) upper-layer, (b) middle-layer, (c) lower-layer, (d) stochastic, (e) natural, and (f) systemic infection. Subpanels 1–4 correspond to light, moderate, severe, and very severe disease levels, respectively. Red numbers indicate preset lesion counts (n represents plant number in scene). The canopy has four layers; lesions occur in the lower, middle, and upper layers (basal leaves disease-free). (For interpretation of the references to colour in this figure legend, the reader is referred to the web version of this article.)

contribution of each canopy layer; stochastic infection tests random distribution; natural infection mimics bottom-up progression; systemic infection (full coverage) serves as an extreme control. Among these patterns, the natural infection pattern follows the vertical lesion distribution rules in Appendix **Table A3**, reflecting realistic bottom-up disease progression.

Lesion numbers were fixed for upper-, middle-, lower-layer, and systemic infections, but varied dynamically with severity for stochastic and natural patterns. Fig. 5 and Fig. 6 show 3D views of maize canopies under these patterns across all severity levels. For simplification, the canopy was vertically divided into four layers by leaf position, with basal leaves assumed disease-free and infections concentrated in lower, middle, and upper layers (specific settings in Fig. 5).

2.4. Construction of Fluspect-B-based LUT

A LUT was constructed with the Fluspect model to retrieve leaf biochemical components across different disease severity levels. The inversion process minimized the root mean square error (RMSE) between measured and simulated reflectance (400–2400 nm). For robust estimation, the final results were the average of the top three parameter sets that yielded the lowest RMSE. The biochemical parameters, their value ranges, and step sizes used for LUT construction are detailed in Table 1.

2.5. Evaluation and validation

To evaluate the accuracy of the coupled maize model in simulating leaf biochemical dynamics under disease stress, we systematically compared model predictions with field measurements. Model performance was assessed using the coefficient of determination (R^2), RMSE, and normalized root mean square error (NRMSE). For disease progression, relative error (RE) quantified the accuracy of DI predictions:

$$R^2 = 1 - \sum_{i=1}^{n} \frac{(y_i - ye)^2}{(y_i - \overline{y})^2}, i = 0, 1, \ldots, n \tag{2a}$$

$$\mathrm{RMSE}(ye\ ,\ y) = \sqrt{\frac{1}{m}\sum_{i=1}^{m}(ye_i - y_i)^2}, i = 0, 1, \ldots, n \tag{2b}$$

$$\mathrm{NRMSE}(ye\ ,\ y) = \frac{\mathrm{RMSE}(ye\ ,\ y)}{\overline{y}} \tag{2c}$$

$$\mathrm{NRMSE1}(ye\ ,\ y) = \frac{\mathrm{RMSE}(ye\ ,\ y)}{y_{max} - y_{min}} \tag{2d}$$

$$\mathrm{RE} = \frac{(DI_{sim} - DI_{obs})}{DI_{obs}} \tag{2e}$$

where y_i, ye_i and $\overline{y}$ represent the measured value, model prediction, and mean of measured values for the i-th sample, respectively; y_{max} and y_{min} denote the maximum and minimum of the measured values. NRMSE1 was normalized by the observed value range to enhance cross-dataset comparability. Following conventional criteria, model performance was classified as: excellent (NRMSE <0.1), good ($0.1 \leq$ NRMSE <0.2), fair ($0.2 \leq$ NRMSE <0.3), and poor (NRMSE ≥ 0.3). DI_{sim} and DI_{obs} represent the simulated and observed disease index, respectively.

3. Results

By integrating disease transmission dynamics with canopy radiative transfer processes, this study systematically deciphers the multi-scale optical response mechanisms of maize under disease stress. We validated the model's environmental response functions, quantified the impact of lesion spatial distribution on canopy reflectance, and established quantitative relationships linking leaf biochemistry to disease severity. This integrated approach ultimately revealed the synergistic response characteristics of canopy reflectance and SIF throughout disease progression. Following this modeling framework, the Results section is organized into five subsections: Sections 3.1–3.3 validate the key modules (disease dynamics, lesion spatial distribution, and leaf optical responses), Section 3.4 evaluates the performance of the integrated model, and Section 3.5 presents the model application to analyze the dynamic evolution of canopy reflectance and SIF during disease progression.

3.1. Optimization and validation of the disease transmission dynamics module

Environmental regulation of the disease transmission process is crucial for developing reliable predictive models. We validated our disease transmission module by comparing simulations of ideal versus environmentally-constrained infections against field observations. Environmentally constrained conditions account for the regulatory effects of temperature, relative humidity, and GDD derived from experimental field data, whereas ideal infection conditions ignore these effects.

Using MNLB as an example, Fig. 7 presents the disease transmission dynamics under both conditions. Under ideal conditions (Fig. 7 a1-a4), the disease spread rapidly, reaching a final DI of 0.83 (Fig. 7 a3). In contrast, under environmentally constrained conditions (Fig. 7 b1-b4), the DI reached only 0.08 (Fig. 7 b3), indicating that environmental factors substantially suppressed both epidemic intensity and transmission rate.

Analysis of host and vector population dynamics further revealed the regulatory mechanisms involved. Under ideal conditions, the susceptible host population (S_m) rapidly transitioned to the infectious state (I_m) with GDD (Fig. 7 a1), while this transition was markedly suppressed under constrained conditions (Fig. 7 b1). Vector population dynamics followed a similar pattern, though their transition process was less affected by environmental factors, with removal occurring primarily through natural mortality (Fig. 7 a2, b2). The basic reproduction number (R_o) and pathogen population (P_o) also showed striking differences: under ideal conditions, R_o stabilized around 410 and continued to increase, with P_o accumulating steadily (Fig. 7 a4), while under constrained conditions, R_o dropped rapidly from an initial value of 190 to 0, with P_o showing a declining trend (Fig. 7 b4).

Simulated disease indices closely matched observations (Table 2), with MCLLS, MSLB, and MNLB errors all under 3%. For MSR, which had no field data, the model estimated a DI of 0.476 under constrained conditions. These results confirm the module's reliability in reproducing field epidemics.

3.2. Effects of lesion spatial distribution patterns on TOC reflectance

While DI quantifies disease severity, it cannot characterize the 3D spatial distribution of lesions within the canopy. We constructed six representative spatial patterns based on natural lesion distribution across severity levels (Section 2.3.5) to systematically evaluate their effects on TOC reflectance.

Comparisons between cmSCOPE-D and LESS simulations confirmed cmSCOPE-D's reliability in simulating canopy reflectance under disease stress (Fig. 8), though LESS produced 13.3%–17.9% higher reflectance values due to differences in radiative transfer algorithms, particularly in handling multiple scattering. LESS simulations used the same Coupled Maize model outputs as cmSCOPE-D, but represented 3D scenes with triangular facets to distinguish the optical properties of healthy and diseased leaves. Solar illumination geometry and sensor viewing geometry were kept identical between the two models. For Coupled Maize model parameters, see Appendix A2.

Lesion spatial distribution significantly influenced canopy reflectance by altering the proportion of healthy and diseased components

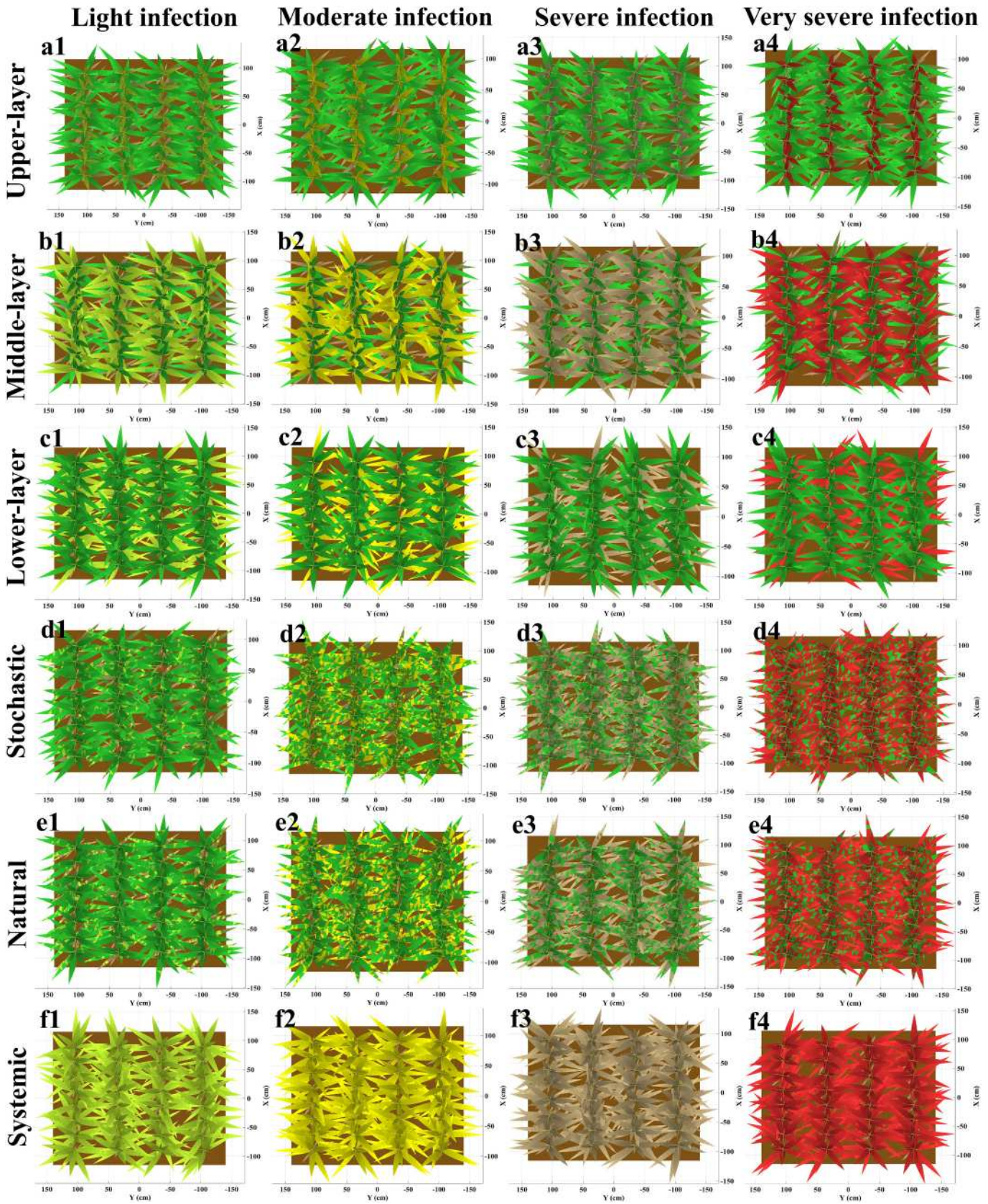


Fig. 6. Top views of maize canopies under different lesion distribution patterns and disease severity levels. Same configurations as in Fig. 5, but shown from a top-down perspective.

Table 1
Parameter settings for the Fluspect-B-based LUT construction.

Parameter	Description	Unit	Range	Step
N	Leaf structure parameter	–	1:2	0.1
C_{ab}	Leaf chlorophyll content	$\mu g/cm^2$	0:80	2
C_{ar}	Leaf carotenoid content	$\mu g/cm^2$	0:15	1
C_w	Leaf water content	g/cm^2	0:0.02	0.002
C_{dm}	Leaf dry matter content	g/cm^2	0.003:0.005	0.0005

within the sensor's field of view. Under light infection (Fig. 8 a1-a2), healthy canopies showed lower visible reflectance but higher NIR and SWIR reflectance than diseased canopies. This pattern is not fully consistent with leaf-level spectral (Fig. 4d); the difference arises from band-dependent factors such as canopy multiple scattering and soil background during upscaling. Influenced by both lesion distribution (Fig. 5 a1-f1) and leaf optical properties, NIR reflectance exhibited the following order: $Ref_{health} > Ref_{natural} > Ref_{stochastic} > Ref_{lower} > Ref_{upper} > Ref_{middle} > Ref_{systemic}$, directly corresponding to lesion proportion within the sensor's view. For instance, although natural and stochastic distributions had identical lesion counts (29*n), the stochastic pattern showed higher lesion proportion in the observation direction (Fig. 6 d1-e1).

Under moderate infection (Fig. 8 b1-b2), natural and stochastic distributions (86*n) approached the lower-layer count (95*n), but their effective lesion proportions ranked as stochastic > natural > lower, resulting in the NIR reflectance sequence: $Ref_{health} > Ref_{lower} > Ref_{natural} > Ref_{stochastic} > Ref_{upper} > Ref_{middle} > Ref_{systemic}$. This pattern persisted under severe and very severe conditions (Fig. 8 c1-d2), with spectral

Table 2
Accuracy assessment of the transmission dynamics model for major maize foliar diseases.

Disease	MCLLS	MSLB	MNLB	MSR
Observed DI	0.410	0.436	0.079	–
Simulated DI	0.402	0.423	0.078	0.476
RE (%)	−1.82	−2.87	−1.27	–

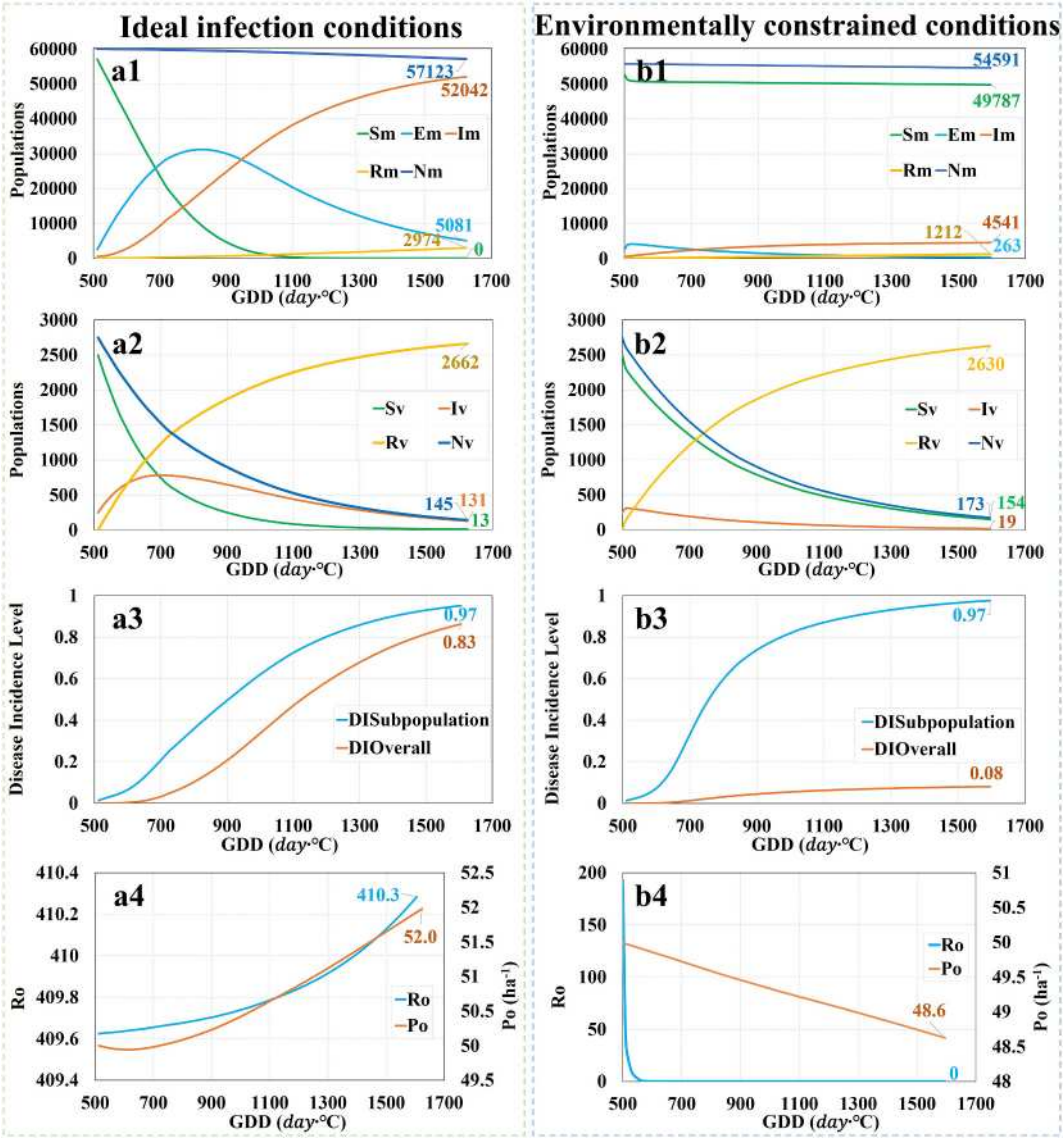


Fig. 7. Disease dynamics of MNLB under ideal (a1-a4) and environmentally constrained (b1-b4) conditions. (a1-b1) Dynamics of maize host subpopulations (S_m: susceptible, E_m: exposed, I_m: infectious, R_m: removed) versus GDD; (a2-b2) Dynamics of vector subpopulations (S_v: susceptible, I_v: infectious, R_v: removed) versus GDD; (a3-b3) Temporal changes in disease severity at population and infected subpopulation levels; (a4-b4) Temporal dynamics of the basic reproduction number (R_o) and pathogen population (P_o).

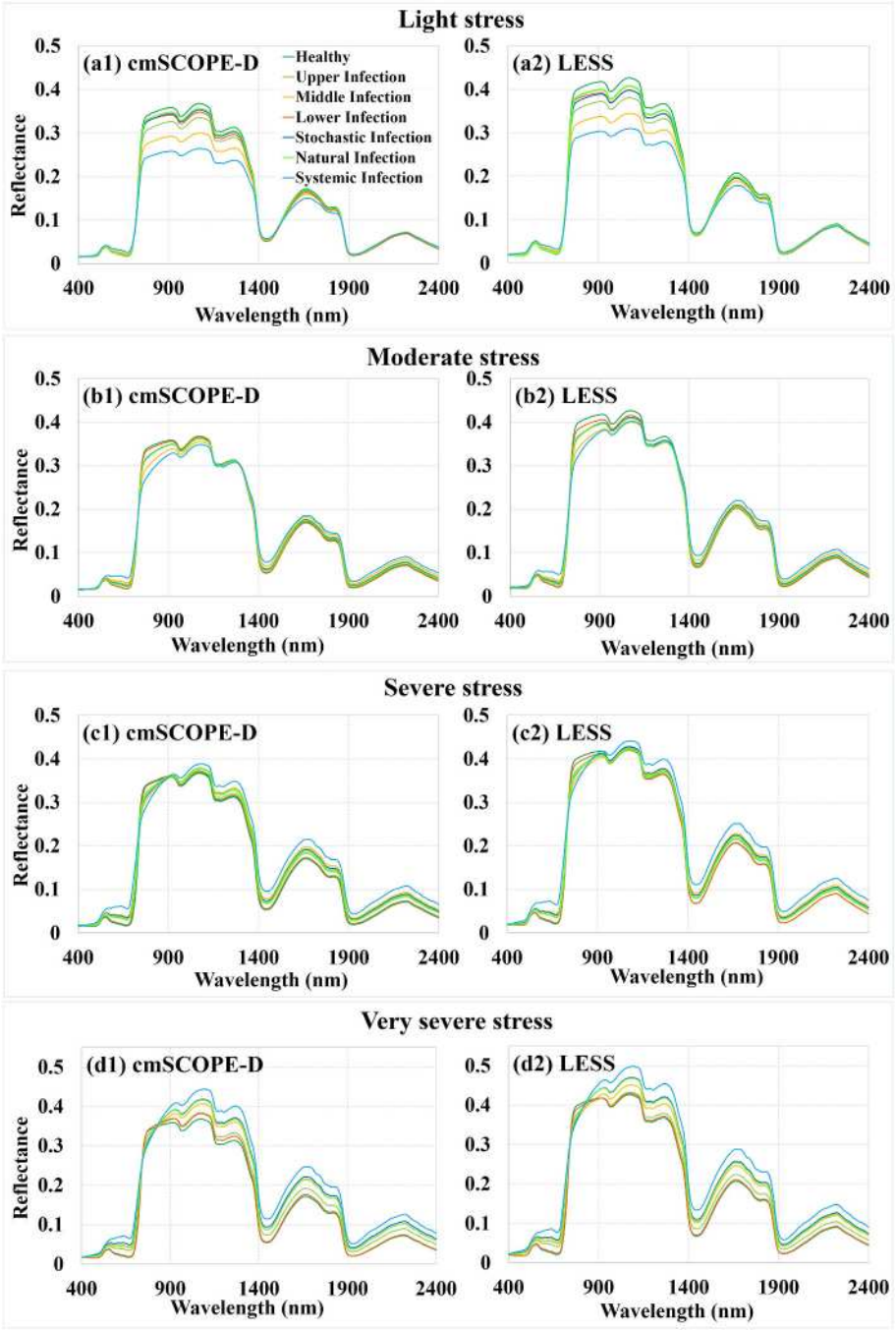


Fig. 8. Effects of lesion spatial distribution patterns on TOC reflectance under different disease severity levels. The figure shows six distribution patterns (upper, middle, lower, stochastic, natural, systemic) at four severity levels: light (a1–a2), moderate (b1–b2), severe (c1–c2), and very severe (d1–d2). Leaf spectra of southern corn rust (MSR) from Fig. 4 are used. Left panels: cmSCOPE-D simulations; right panels: LESS simulations.

differences amplifying as lesions spread to middle and upper canopy layers. Natural and stochastic distributions yielded the most similar results, particularly at advanced stages when natural pattern lesions expanded into mid-to-upper canopy.

Vertical stratification analysis revealed that middle-layer lesions contributed most strongly to reflectance variations (**Fig. A 5**). Compared to erect upper leaves (Fig. 6 a1-a4) and shaded lower leaves (Fig. 6 c1-c4), the relatively horizontal middle leaves (Fig. 6 b1-b4) had the largest projection in the vertical view direction, producing the strongest spectral response across severity levels.

Spectral responses exhibited systematic wavelength-dependent variations. Visible reflectance increased monotonically with severity for all patterns, while NIR and SWIR regions showed non-monotonic trends—initially decreasing then increasing (**Fig. A 5**). NIR-based sensitivity analysis indicated the response intensity ranking: $Sen_{systemic} > Sen_{middle} > Sen_{stochastic} > Sen_{natural} > Sen_{upper} > Sen_{lower}$. These results highlight the crucial role of 3D lesion spatial distribution in modulating canopy reflectance and provide theoretical support for developing multi-angle remote sensing approaches to retrieve disease distribution patterns.

3.3. Modeling and validation of leaf optical responses to disease stress

To accurately simulate canopy spectral characteristics under disease,

we developed a leaf optical property model that quantifies changes according to disease severity. This section is organized into three subsections following the technical workflow: first establishing empirical relationships between biochemical parameters and disease severity (Section 3.3.1), then validating biochemical retrieval accuracy (Section 3.3.2), and finally evaluating leaf spectral simulation accuracy (Section 3.3.3). Specifically, we used a LUT constructed with Fluspect-B to retrieve biochemical parameters from the measured spectra of diseased leaves, established and validated empirical functions describing how these parameters vary with DI against field-measured biochemical data, and finally evaluated model performance by comparing simulated and measured leaf spectra, thereby providing reliable leaf-level inputs for subsequent canopy-scale simulations (see Section 3.4).

3.3.1. Responses of leaf biochemical components to disease stress

Regression analysis between measured biochemical components and DI revealed significant responses to disease stress (Table 3). Specifically, pigment components (C_{ab} and C_{ar}) exhibited strong exponential decay relationships with DI ($R^2 = 0.591–0.915$), indicating rapid decline with disease progression and highlighting their high sensitivity to infection. C_{dm} also decreased exponentially but with variable goodness-of-fit ($R^2 = 0.105–0.520$). In contrast, C_w showed weaker linear negative correlations with DI ($R^2 = 0.126–0.760$), reflecting the complex interaction between disease effects and environmental factors on water status.

Regression equations between LUT-derived biochemical parameters and DI further demonstrated strong relationships (Table 4). Despite the limited sample size (covering five severity levels from healthy to very severe), the regression models exhibited high explanatory power ($R^2 = 0.885–0.998$). Notably, the leaf structure parameter N exhibited a significant quadratic relationship with DI, demonstrating a dynamic, nonlinear response to disease stress. These validated regression functions (Table 4) were integrated into the disease transmission dynamics module to drive the evolution of leaf optical properties, providing a robust foundation for subsequent optical modeling. Based on these empirical relationships (Table 4), the accuracy of biochemical retrieval is evaluated in Section 3.3.2 and Fig. 9.

Table 3
Regression equations between measured biochemical constituents and disease severity.

Disease	Biochemical Component	Regression Equation	R^2	Sample Size
MCLLS	C_{ab}	$C_{ab} = 52.645*\exp.(-0.977*DI)$	0.781	40
	C_{ar}	$C_{ar} = 11.775*\exp.(-1.192*DI)$	0.765	
	C_w	$C_w = -0.0029*DI + 0.0127$	0.206	
	C_{dm}	$C_{dm} = 0.0043*\exp.(-0.161*DI)$	0.218	
MSLB	C_{ab}	$C_{ab} = 58.964*\exp.(-2.382*DI)$	0.727	40
	C_{ar}	$C_{ar} = 11.598*\exp.(-1.284*DI)$	0.591	
	C_w	$C_w = -0.0064*DI + 0.0107$	0.176	
	C_{dm}	$C_{dm} = 0.0041*\exp.(-0.122*DI)$	0.105	
MNLB	C_{ab}	$C_{ab} = 44.712*\exp.(-2.885*DI)$	0.898	24
	C_{ar}	$C_{ar} = 9.9229*\exp.(-2.26*DI)$	0.915	
	C_w	$C_w = -0.0053*DI + 0.0121$	0.126	
	C_{dm}	$C_{dm} = 0.0043*\exp.(-0.172*DI)$	0.128	
MSR	C_{ab}	$C_{ab} = 47.602*\exp.(-2.331*DI)$	0.826	8
	C_{ar}	$C_{ar} = 10.546*\exp.(-1.585*DI)$	0.864	
	C_w	$C_w = -0.0126*DI + 0.0134$	0.760	
	C_{dm}	$C_{dm} = 0.0045*\exp.(-0.352*DI)$	0.520	

Table 4
Regression equations between inverted biochemical constituents and disease severity.

Disease	Biochemical Component	Regression Equation	R^2	Sample Size
MCLLS	C_{ab}	$C_{ab} = 50.614*\exp.(-0.955*DI)$	0.988	5
	C_{ar}	$C_{ar} = 11.377*\exp.(-1.153*DI)$	0.996	
	C_w	$C_w = -0.0053*DI + 0.0128$	0.885	
	C_{dm}	$C_{dm} = 0.0043*\exp.(-0.291*DI)$	0.951	
	N	$N = 0.6219*DI^2–0.4595*DI + 1.1965$	0.982	
MSLB	C_{ab}	$C_{ab} = 47.219*\exp.(-2.459*DI)$	0.991	5
	C_{ar}	$C_{ar} = 11.503*\exp.(-1.422*DI)$	0.994	
	C_w	$C_w = -0.0117*DI + 0.0132$	0.989	
	C_{dm}	$C_{dm} = 0.0043*\exp.(-0.319*DI)$	0.941	
	N	$N = 1.0048*DI^2–0.4289*DI + 1.1925$	0.992	
MNLB	C_{ab}	$C_{ab} = 51.05*\exp.(-2.964*DI)$	0.990	5
	C_{ar}	$C_{ar} = 11.346*\exp.(-2.339*DI)$	0.998	
	C_w	$C_w = -0.014*DI + 0.0133$	0.987	
	C_{dm}	$C_{dm} = 0.0043*\exp.(-0.319*DI)$	0.941	
	N	$N = 0.9701*DI^2–0.3994*DI + 1.1908$	0.984	
MSR	C_{ab}	$C_{ab} = 47.193*\exp.(-2.635*DI)$	0.996	5
	C_{ar}	$C_{ar} = 11.199*\exp.(-1.731*DI)$	0.994	
	C_w	$C_w = -0.0155*DI + 0.0126$	0.991	
	C_{dm}	$C_{dm} = 0.0043*\exp.(-0.319*DI)$	0.941	
	N	$N = 0.2312*DI^2 + 0.0582*DI + 1.2666$	0.940	

Note: Table 4 is based on inversion of averaged leaf spectra for five severity levels (healthy, light, moderate, severe, very severe), corresponding to DI values of 0, 0.1, 0.3, 0.5, and 0.7, respectively ($n = 5$ per disease). In contrast, Table 3 uses whole-plant DI with directly measured biochemical components ($n = 40/40/24/8$). The two tables thus differ in data source, scale, and measurement method, serving different purposes: Table 4 drives leaf optical property evolution in the disease module, while Table 3 validates whole-plant performance.

3.3.2. Accuracy assessment of biochemical component predictions

To evaluate prediction accuracy of biochemical components under four maize diseases, we calculated predicted values using the empirical equations in Table 4, took the measured values from the discrete leaf samples in Table 3 as reference, and generated scatterplots of measured versus predicted values (Fig. 9), with quantitative analysis using RMSE, NRMSE, and NRMSE1. Overall, the model achieved high predictive accuracy for C_{ab}, C_{ar}, and C_{dm}, with NRMSE ranges of 0.089–0.197, 0.109–0.173, and 0.027–0.163, respectively (all below 0.2). Predictions for C_w were less accurate (NRMSE: 0.009–0.279). Further evaluation using NRMSE1 confirmed that C_{ab} and C_{ar} maintained low values (0.103–0.175), while C_w and C_{dm} showed substantially higher uncertainties (0.321–0.670), indicating greater prediction uncertainty for water and dry matter components.

Analysis by disease type (Fig. 9) showed optimal prediction performance for MCLLS (NRMSE = 0.071–0.109; NRMSE1 = 0.132–0.363), though with systematic overestimation of C_w and C_{dm}. Predictions for MSLB were also reliable (NRMSE = 0.056–0.197; NRMSE1 =

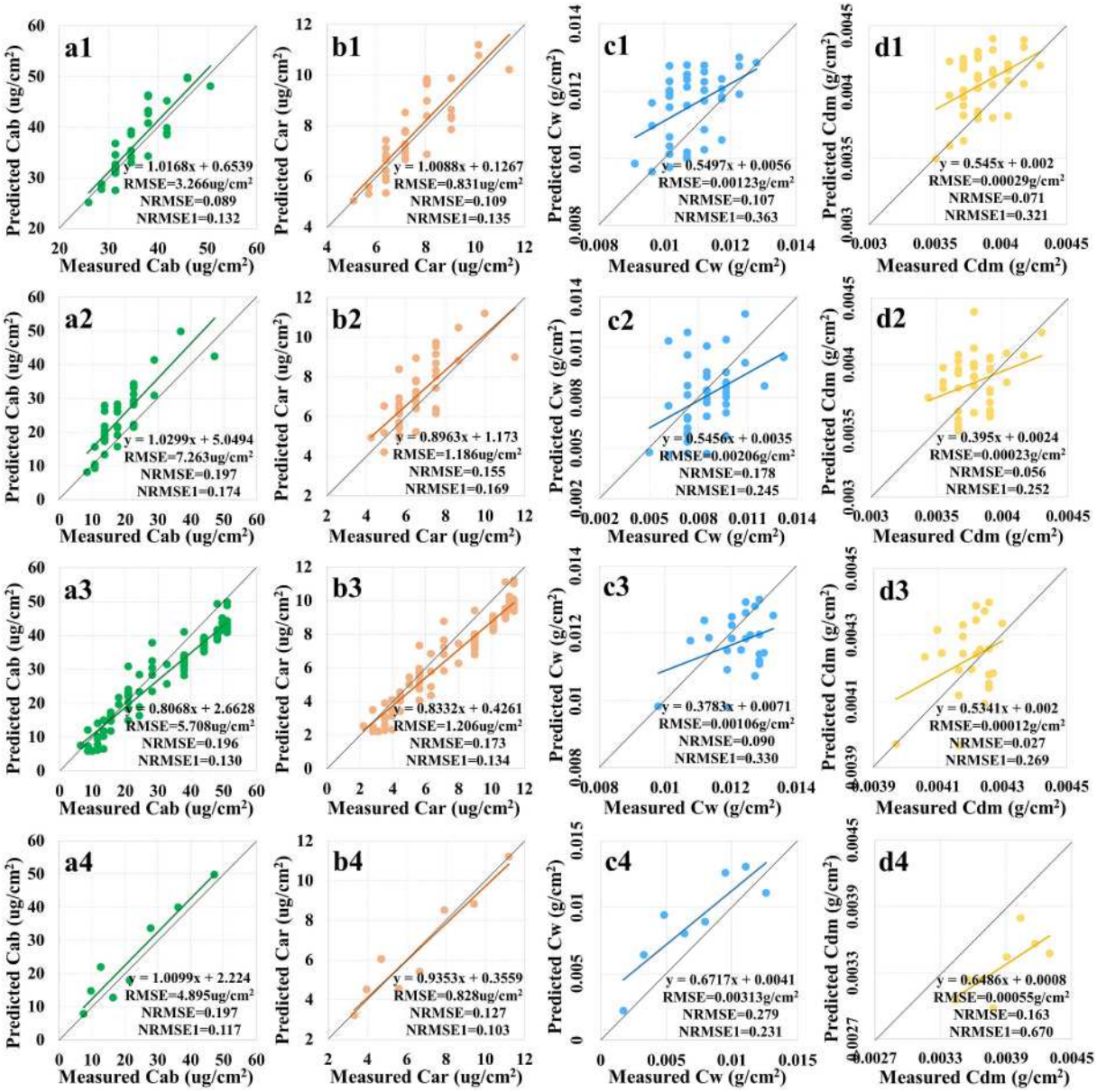


Fig. 9. Measured versus predicted leaf biochemical components for four maize diseases. The predicted values are calculated using the regression equations derived from spectral inversion (Table 4). (a1-d1: MCLLS, n = 40; a2-d2: MSLB, n = 40; a3-d3: MNLB, n = 24; a4-d4: MSR, n = 8).

0.174–0.252), with overall overestimation of C_{ab} and C_{ar}, and systematic bias for C_w and C_{dm} (underestimation at high values, overestimation at low values). MNLB predictions maintained high accuracy (NRMSE = 0.027–0.196; NRMSE1 = 0.130–0.330), though C_{ab}, C_{ar}, and C_w were underestimated at high values while C_{dm} was overestimated at low values. For MSR, C_{ab} and C_{ar} predictions remained accurate (NRMSE = 0.127–0.197; NRMSE1 = 0.103–0.117), but C_w and C_{dm} showed larger errors (NRMSE = 0.163–0.279; NRMSE1 = 0.231–0.670), with overall overestimation of C_{ab} and C_w and underestimation of C_{dm}. This apparent paradox—high R^2 values for MSR in Table 3 (Cdm: 0.520; Cw: 0.760) yet large prediction errors—is primarily attributable to the small sample size (n = 8), which tends to produce extreme but unstable regression relationships. However, disease-specific physiological effects cannot be completely ruled out. Multiple evaluation metrics confirmed the model's stable capability to capture C_{ab} and C_{ar} dynamics across disease conditions, though limitations remain in predicting water and dry matter components.

3.3.3. *Accuracy assessment of leaf spectral simulations*

To evaluate the accuracy of leaf spectral simulation under disease stress, biochemical values retrieved for five severity levels were input into Fluspect-B to simulate spectral characteristics and compared against measurements (Fig. 10). Disease severity was categorized into five levels (healthy, light, moderate, severe, and very severe), corresponding to DI values of 0, 0.1, 0.3, 0.5, and 0.7, respectively. Comprehensive analysis revealed systematic performance variations across severity levels, disease types, and spectral regions:

(1) Higher accuracy for light to moderate stress than for severe stress. For healthy to moderate infection stages (Fig. 10 a1-d3), simulated spectra closely matched measurements, whereas accuracy declined markedly under severe stress (Fig. 10 a4-d5). This primarily results from complex alterations in leaf biochemistry and cellular structure under high disease stress, while traditional radiative transfer models like Fluspect-B incorporate only limited

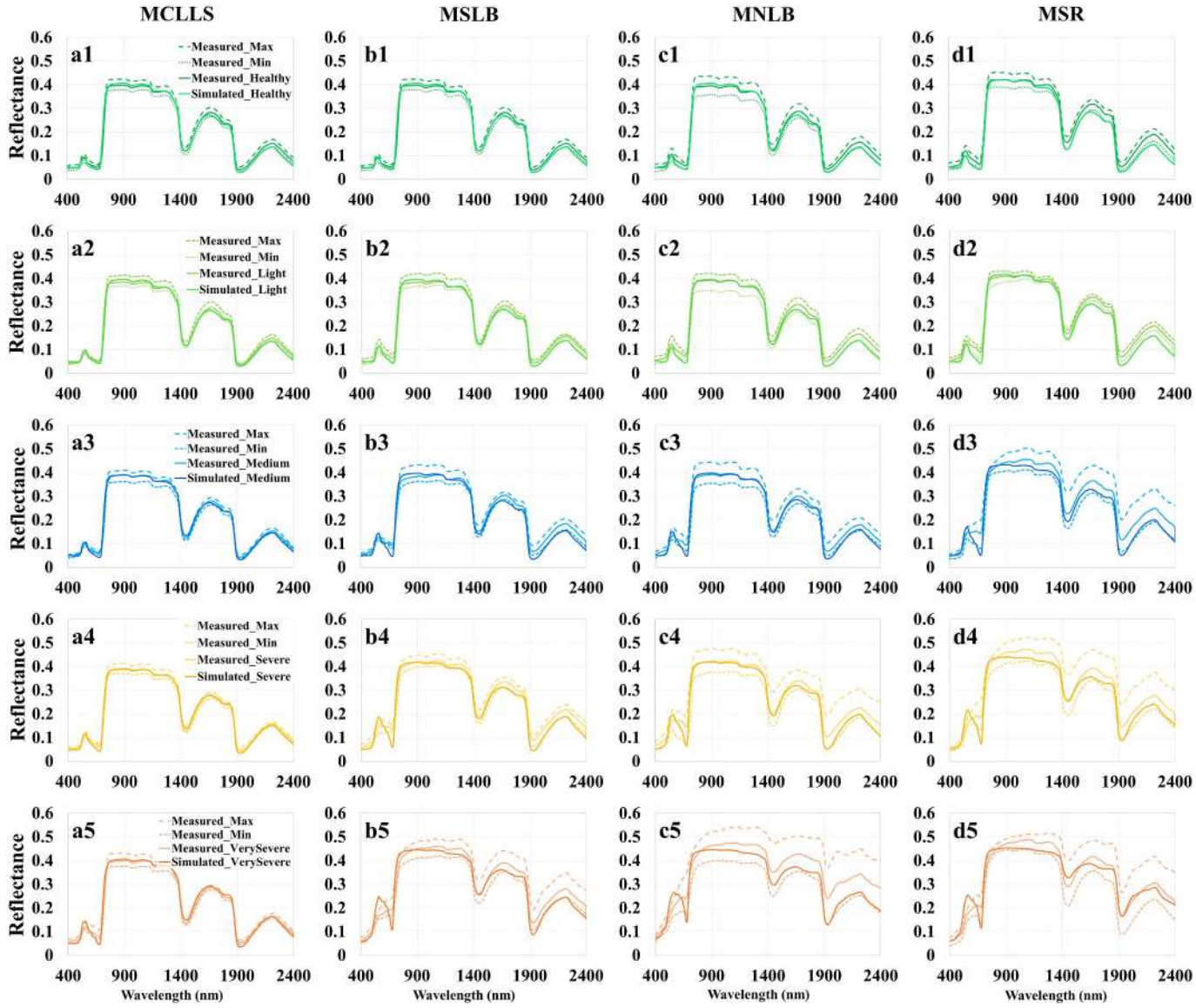


Fig. 10. Comparison of measured and simulated leaf reflectance spectra across severity levels for four maize diseases (a-d: MCLLS, MSLB, MNLB, MSR; 1–5: healthy, light, moderate, severe, very severe).

biochemical parameters and typical structural assumptions, failing to capture disease-specific spectral anomalies.

(2) Higher accuracy for low-destructiveness diseases. The model achieved best performance for MCLLS (Fig. 10 a1-a5), where disease-induced structural changes are minimal. In contrast, more destructive diseases (MSLB, MNLB, MSR; Fig. 10 b1-d5) produced larger deviations, as they cause lesion expansion, tissue destruction, and sporulation that existing models cannot adequately represent.

(3) Higher accuracy in NIR than visible or SWIR regions. In the NIR, where spectra are primarily controlled by structure parameter N, fitting was satisfactory across all diseases, though discrepancies increased under high severity (e.g., Fig. 10 d3-d5). In the SWIR, where spectra are jointly influenced by N, C_w, and C_{dm}, simulations were generally acceptable but exhibited clear deviations under severe infection (e.g., Fig. 10 c5-d5). In the visible region, despite relatively accurate pigment predictions, overall spectral reproduction was weaker, showing anomalous absorption peaks around 660–690 nm and amplified errors at higher severity (e.g., Fig. 10 c3-d5). These limitations reflect insufficient representation of disease-specific biophysical changes and associated biochemical responses in existing models.

3.4. Simulation and accuracy assessment of canopy optical properties under disease stress

Using the cmSCOPE-D model, we simulated and validated TOC reflectance under MCLLS, MSLB, and MNLB stresses. The cmSCOPE-D model employed vertically heterogeneous distributions of leaf angle and iLAI across four vertical layers. The disease transmission dynamics module adopted a natural infection pattern, incorporating environmental regulation by temperature and relative humidity (specific parameters in **Table A 4**). Fig. 11 compares simulated and measured TOC reflectance, where panels (a), (b), and (c) correspond to MCLLS (LAI = 3.8), MSLB (LAI = 3.8), and MNLB (LAI = 3.2), respectively.

Overall, the model successfully reproduced canopy spectral characteristics under disease stresses, showing strong agreement with measurements in the 400–620 nm blue-to-orange region (capturing pigment absorption) and 780–920 nm (due to multi-level structural scattering properties). However, systematic underestimation occurred in the

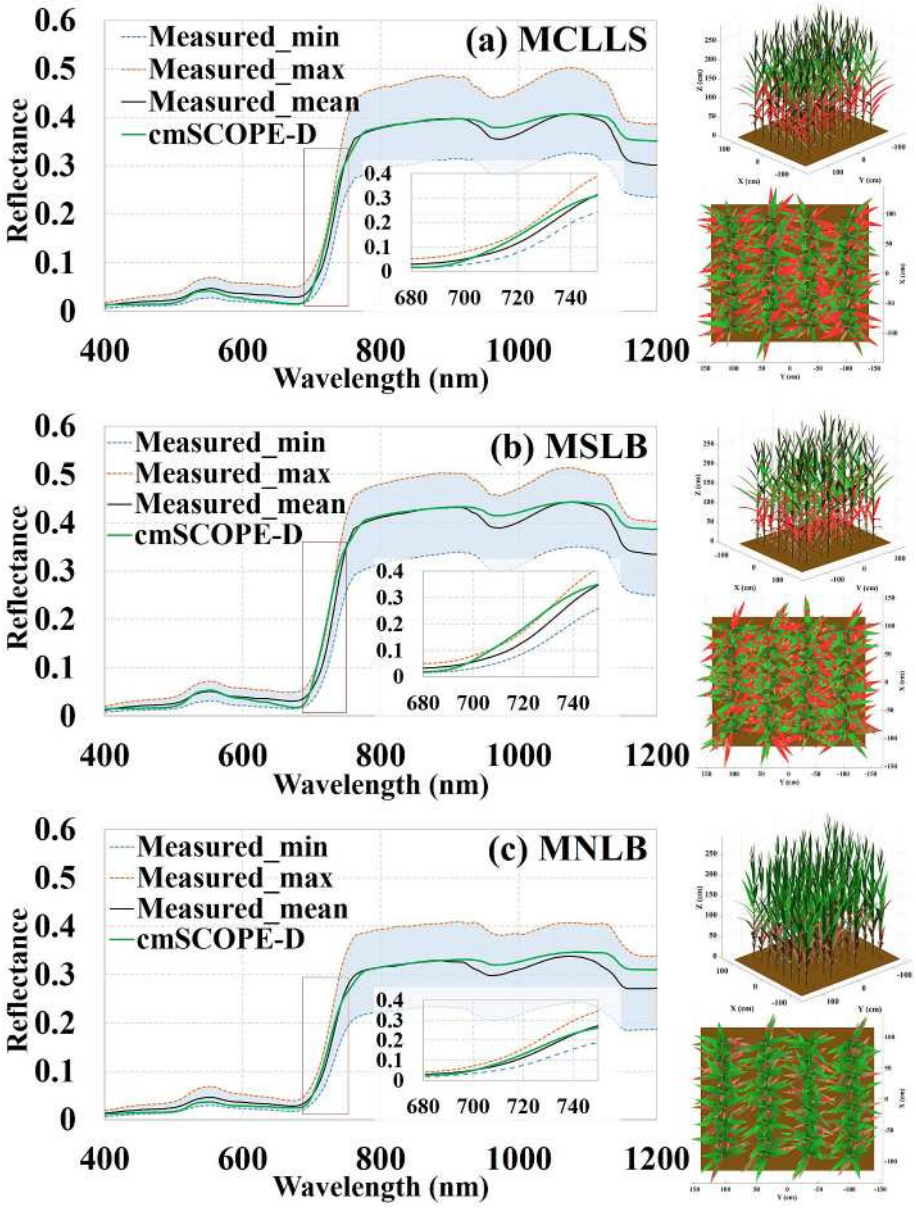


Fig. 11. Validation of canopy reflectance simulations under disease stress. Panels a–c: MCLLS, MSLB, MNLB. Left: measured vs. simulated reflectance (red-edge 680–740 nm enlarged). Right: side and top views of simulated canopy 3D scenes. (For interpretation of the references to colour in this figure legend, the reader is referred to the web version of this article.)

650–680 nm red band, while overestimation appeared in the 700–740 nm red-edge region and 930–1200 nm SWIR bands. These discrepancies stem from inherent errors in simulating disease-stress leaf optical properties and model underestimation of C_w with red and red-edge regions particularly affected by disease-induced chlorophyll degradation and cellular disruption not fully captured by current models.

Model accuracy decreased with increasing disease severity. Under light infection (e.g., MNLB with DI = 0.078, Fig. 11c), simulated spectra matched measurements well. In contrast, under moderate to severe infection (e.g., MCLLS with DI = 0.402, Fig. 11a; MSLB with DI = 0.423, Fig. 11b), simulation errors increased, indicating limitations in representing biochemical parameter dynamics during disease progression.

In summary, while the cmSCOPE-D model demonstrates capability in simulating canopy optical properties under disease stress, it exhibits significant biases remain in physiologically sensitive spectral regions and under moderate to severe disease severity. Future improvements should focus on enhancing the representation of dynamic changes in key components with disease severity, and developing leaf optical models that incorporate disease-specific spectral features.

3.5. *Dynamic simulation of TOC reflectance and SIF signals under disease stress*

This section employs the cmSCOPE-D model to simulate maize canopy dynamics under disease stress, comparing progression between environmentally constrained and ideal infection conditions. Fig. 12, **Fig. A 6**, **Fig. A 7** and **Fig. A 8** present simulation results for MCLLS, MSLB, MNLB, and MSR, respectively, illustrating biochemical components, 3D canopy scenes, TOC reflectance, and SIF signals, with emphasis on red-edge and SIF peak band responses. Subpanels (a) and (b) display constrained and ideal conditions, respectively.

Environmental factors significantly controlled over disease development. Under ideal conditions, all four diseases reached DI = 0.83, substantially exceeding constrained values (0.412, 0.435, 0.081, and

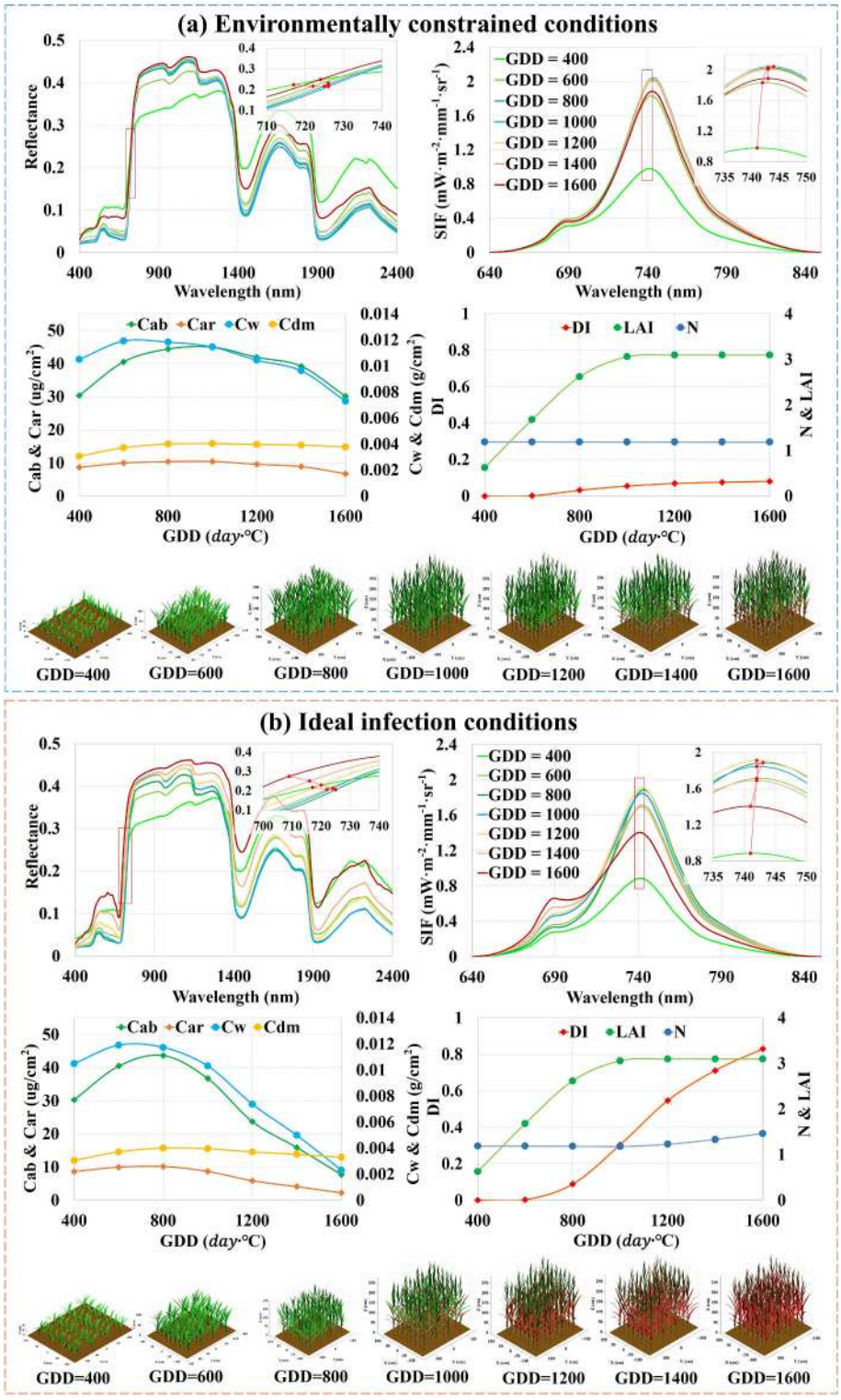


Fig. 12. Dynamic changes in maize canopy biochemical components, reflectance, and SIF under MNLB stress. The figure compares simulation results under environmentally constrained (a) and ideal infection (b) conditions, including: TOC reflectance heatmaps (red-edge 710–740 nm enlarged) and SIF spectra (735–750 nm enlarged); canopy physicochemical parameters and LAI as functions of GDD; and 3D canopy scenes (lesions shown in red). (For interpretation of the references to colour in this figure legend, the reader is referred to the web version of this article.)

0.491). Biochemical components and LAI dynamics were co-regulated by genotype and disease: during early to mid-vegetative growth (GDD $\leq$ 800 day•°C), all components gradually accumulated to peak values; entering late vegetative growth (GDD $>$ 800 day•°C), components began to decline under combined senescence and disease effects, with accelerated decline during reproductive growth.

The cmSCOPE-D model successfully captured three key canopy responses:

(1) Disease stress induced full-spectrum reflectance increase and red-edge blue-shift. Under ideal conditions (Fig. 12-**Fig. A 8**b), canopy reflectance exhibited distinct phasic changes. When GDD $\leq$ 800 day•°C, visible reflectance decreased due to enhanced chlorophyll absorption, while NIR reflectance increased with canopy development, accompanied by progressive red-edge red-shift. When GDD $>$ 800 day•°C, combined disease and senescence effects caused pigment degradation and structural damage, leading to systematic reflectance increase (particularly in visible bands) and a transition from red-shift to blue-shift in the red-edge position, forming a "$>$"-shaped trajectory. This blue-shift closely correlated with chlorophyll reduction, serving as a spectral indicator of canopy health deterioration. Under constrained conditions (Fig. 12-**Fig. A 8**a), although a similar red-shift to blue-shift transition occurred, the blue-shift magnitude was significantly smaller and reflectance increases were more moderate, indicating effective disease suppression and maintained canopy physiological function.

(2) Disease stress caused SIF intensity decline and peak wavelength blue-shift. SIF responses demonstrated higher sensitivity and complexity than reflectance. Using MSLB as an example (**Fig. A 7**b), under ideal conditions the SIF peak wavelength showed a cross-trajectory of "red-shift followed by blue-shift." When GDD $\leq$ 600 day•°C, the SIF peak red-shifted with canopy growth and pigment accumulation; during 600 $<$ GDD $\leq$ 1000 day•°C, dense canopy enhanced fluorescence reabsorption, suppressing red-edge SIF signals and shifting the peak to 743 nm; under severe stress (GDD $>$ 1000 day·°C), SIF exhibited two critical changes: overall intensity decline and distinct peak blue-shift. This blue-shift primarily resulted from reduced fluorescence reabsorption capacity due to chlorophyll degradation. Under disease stress, decreased pigment content reduced canopy reabsorption of red fluorescence, allowing more short-wavelength fluorescence to escape, manifesting as SIF peak shift toward shorter wavelengths. The concurrent SIF blue-shift and reflectance red-edge blue-shift jointly confirmed pigment degradation. Under constrained conditions, the SIF peak showed only an initial red-shift without significant blue-shift or crossover trajectory, reflecting milder disease severity.

(3) Scale transfer of spectral features and disease-specific responses revealed consistent patterns from leaf to canopy scales. The systematic reflectance increase with disease severity observed at leaf level was consistently reproduced at canopy scale, demonstrating scale-invariant spectral responses induced by pigment degradation and structural damage. Under ideal conditions (DI = 0.83), canopy optical response intensity varied among diseases: MSR induced the most pronounced red-edge blue-shift and SIF peak blue-shift, followed by MNLB, MSLB, and MCLLS. This sequence aligned with disease destructiveness, indicating that stronger disease specificity induces more distinct spectral and fluorescence changes. Reflectance and SIF jointly indicated canopy health from structural and photosynthetic perspectives, respectively, with their synergistic patterns providing a theoretical basis for multi-spectral and fluorescence remote sensing of crop diseases.

4. Discussion

4.1. Advantages and validation

This study establishes a disease transmission dynamics module for the cmSCOPE framework by coupling with the SEIR model, enabling a complete radiative transfer simulation from pathogen infection to canopy optical response. The core advantage of this module is its mechanistic and dynamic nature. Compared with previous studies (Zhang et al., 2019) that relied on statistical relationships between disease severity and spectral indices, our module has the advantage of quantifying the influence of environmental factors like temperature and humidity on disease transmission. This advantage allows for differentiated simulation of epidemic trajectories, mapping dynamic disease development to observable changes in canopy reflectance and SIF signals (Fig. 7).

Model reliability was demonstrated through multi-scale validation against field measurements. At the population level, simulated disease indices showed strong agreement with field observations, with relative errors below 3% for major diseases (Table 2). For leaf optical properties, the Fluspect-B-based biochemical retrieval model reliably captured the variations of major pigment components under different disease severity levels (Fig. 9). The retrieval achieved high accuracy for chlorophyll and carotenoids (NRMSE $<$0.2), leading to spectral simulations that closely matched measurements under light-to-moderate infection severity (Fig. 10).

Recognizing the established capability of the 3D radiative transfer model LESS in representing complex canopy structures, we employed it as a reference benchmark to evaluate the ability of cmSCOPE-D in simulating the impact of 3D lesion distribution on canopy reflectance. The close match in spectral morphology between cmSCOPE-D and LESS simulations (Fig. 8) indicates that our model effectively captures the variation patterns in canopy reflectance induced by different lesion distribution patterns, thereby supporting its reliability in representing this core mechanistic aspect.

These comprehensive validations demonstrate that after equipping the disease transmission dynamics module, the cmSCOPE-D model can effectively elucidate optical response mechanisms under disease stress and provides a reliable foundation for remote sensing-based crop disease monitoring.

4.2. Lesion spatial distribution: a hitherto underappreciated modulator

TOC reflectance simulation results confirmed that the three-dimensional spatial distribution of lesions is a key determinant of canopy reflectance, independent of overall disease severity (Section 3.2). Specifically, lesions located on middle-layer leaves exert the greatest impact on canopy reflectance, primarily due to their maximal projected area in the vertical viewing direction. This explains why the disease severity assessed by field-level visual inspection (which focuses more on the overall plant condition) sometimes diverges from remote sensing–derived results: sensors more directly capture the proportion of healthy versus diseased tissues within their field of view, especially at the canopy mid-layer (Baret et al., 2010).

This finding has important implications for remote sensing–based disease monitoring (Zhao et al., 2023) and echoes the insights from canopy radiative transfer theory regarding the sensitivity of optical signals to the spatial arrangement of components (Widlowski et al., 2015). Traditionally, the DI has been regarded as the core metric for assessing severity; however, our results demonstrate that canopies with identical DI values but different lesion distribution patterns can exhibit markedly different reflectance spectra (Fig. 8, **Fig. A 5**). Additionally, the development of next-generation, high-accuracy disease monitoring models must account for the 3D heterogeneity of lesion distribution. Integrating multi-angular remote sensing observations may offer new opportunities for retrieving the spatial distribution patterns of disease within the canopy.

4.3. From leaves to canopy: scaling of spectral responses and model limitations

This study demonstrates the scaling of spectral responses from leaf to canopy under disease stress. The increasing reflectance across all wavelengths with disease severity observed at leaf scale was consistently reproduced in canopy-scale simulations, confirming the scale-invariant nature of spectral changes induced by pigment degradation and

cellular damage. However, model accuracy declined under severe diseases due to limitations at three critical levels.

First, at the leaf scale, generic radiative transfer models like Fluspect cannot capture disease-specific biophysical alterations, and pustule formation, tissue necrosis, and secondary pigment accumulation exceed current parameterization scope(Liu et al., 2023). Second, at the canopy scale, the framework does not yet incorporate quantitative response relationships of structural parameters to the combined effects of senescence and disease stress, specifically disease-driven alterations in leaf angle distribution and area reduction from abscission. This causes systematic biases in late-growth simulations: overestimation in red-edge to SWIR regions and underestimation in visible bands, consistent with radiative transfer theory where leaf drooping and area reduction alter multiple scattering and light interception. Third, the reliability of the empirical relationships between DI and leaf biochemical components is constrained by relatively small and unevenly distributed sample sizes. The regression equations in Table 4 have low degrees of freedom, which is insufficient to fully demonstrate the model's robustness under broader conditions. The DI values in Table 3 are mainly concentrated in the light-to-moderate range, thereby limiting the model's applicability to severe and very severe disease levels.

Future enhancements can advance along two pathways, while also addressing the data limitations. For leaf optical modeling, empirical spectral vectors (GSV-L model (Ma and Fang, 2023) or PCA-based methods (Liu et al., 2017)) enable rapid characterization, while advanced physical models accounting for disease-induced changes in surface roughness and internal scattering (e.g., adaxial–abaxial leaf models (Ran et al., 2025)) strengthen mechanistic foundations—aligning with efforts to adapt leaf radiative transfer models to stress conditions (Féret et al., 2017). For canopy representation, quantitative relationships between disease stress and structural parameters (leaf inclination distribution, leaf area dynamics) must be established and integrated into radiative transfer frameworks. Meanwhile, future studies should collect more balanced datasets covering a wider range of DI values (especially severe and very severe levels) and validate or refine the DI-biochemistry relationships across different maize cultivars and environmental conditions.

This coordinated leaf-to-canopy co-optimization strategy, together with improved empirical parameterization, should substantially improve model accuracy under severe disease conditions, providing more reliable mechanistic support for remote sensing–based crop disease monitoring.

4.4. SIF as an early and physiological indicator of disease stress

This study successfully simulated the unique response of solar-induced chlorophyll fluorescence (SIF) to disease stress, characterized by an initial red-shift followed by a blue-shift in peak wavelength, accompanied by a significant intensity decline (Section 3.5). This complex SIF behavior demonstrates higher sensitivity than traditional reflectance-based metrics, highlighting SIF's considerable potential for early disease detection (Wang et al., 2023; Xu et al., 2021; Zeng et al., 2022). Since SIF emission is jointly modulated by leaf physiological status, canopy structural properties, and illumination-observation geometries (Wang et al., 2023), fully exploiting the physiological information embedded in SIF signals is crucial for elucidating disease stress mechanisms and revealing plant physiological alterations under stress (Du et al., 2023; Jing et al., 2022).

From a physiological perspective, the initial increase and subsequent decrease in SIF reflect the synergistic effects of maize growth and disease stress: during the early stage, rapid growth leads to increases in LAI and pigment accumulation, and SIF rises with canopy development; during the late stage, senescence and disease jointly accelerate pigment degradation and tissue necrosis, leading to a decline in SIF. Differences in SIF trajectories among diseases (e.g., MSR shows more pronounced changes than MCLLS) may arise from pathogen-specific effects on the photosynthetic apparatus.

However, current modeling frameworks primarily incorporate non-physiological factors affecting SIF, with limited systematic incorporation of physiological regulatory mechanisms (Wang et al., 2023). Notably, the assumption of a constant maximum carboxylation rate (Vcmax25) throughout the growing season and across disease stress conditions contradicts reality, as Vcmax25 is strongly regulated by biotic and abiotic stresses and exhibits pronounced seasonal dynamics (Prikaziuk et al., 2023; Song et al., 2021).

Therefore, developing dynamic response functions for key physiological parameters such as Vcmax25 under disease stress and embedding them into the SIF simulation framework represents an essential step toward enhancing both physiological interpretability and predictive accuracy for crop disease monitoring applications. It should be noted that, due to equipment limitations, no SIF measurements were acquired in this study for direct validation. Although the simulated SIF dynamics are qualitatively consistent with the observed red-edge shifts, direct validation remains to be carried out in future work with simultaneous SIF and reflectance measurements.

4.5. Model application prospects and future directions

The cmSCOPE-D model provides a versatile simulation tool for characterizing maize canopy optical properties across growth stages and stress conditions. Its primary application lies in establishing a mechanistic understanding for multi-source remote sensing-based crop disease monitoring, early detection, and loss assessment, particularly through integrated hyperspectral and SIF observations, supporting sustainable crop protection strategies.

Furthermore, forward modeling will serve the retrieval of disease severity. Xue et al. (2026) successfully retrieved disease severity by linearly mixing lesion and healthy spectra in proportion using an extended PROSAIL model, highlighting the fundamental support that well-validated forward models provide for inversion(Xue et al., 2026). As a next step, we plan to use cmSCOPE-D to generate synthetic data and explore methods to improve the retrieval accuracy of DI and lesion spatial distribution.

Future research priorities include model refinement, parameter optimization and generalization, and framework extension. Model refinement includes developing disease-specific leaf optical models, incorporating dynamic physiological parameters, and accounting for canopy structural alterations induced by both senescence and disease stress. Model parameters require optimization and validation using more extensive datasets encompassing diverse disease types, crop genotypes, and environmental conditions to enhance model robustness and transferability. Building upon the cmSCOPE framework, this modeling paradigm should be extended to other staple crops such as wheat and rice, ultimately establishing a generic Coupled Crop-RTMs System. Through these developments, the modeling framework will provide reliable support for smart agriculture and global food security.

5. Conclusions

The cmSCOPE-D model establishes the full-chain simulation framework connecting infection to leaf-canopy optical responses by coupling disease transmission dynamics with radiative transfer processes. This integrated approach enables systematic characterization of multi-scale optical properties in diseased maize, with validation across disease index, leaf biochemistry, and leaf-canopy spectral reflectance demonstrating strong accuracy. Our results reveal that three-dimensional lesion spatial distribution critically modulates canopy optical signals, with solar-induced fluorescence (SIF) exhibiting a distinctive “intensity decline-peak blue-shift” pattern that shows superior disease sensitivity compared to reflectance red-edge shifts. While severe disease conditions expose limitations in current leaf-scale disease representations, this mechanistic framework provides novel theoretical support for remote

sensing-based crop disease monitoring. These findings advance understanding of disease-induced optical responses and establish foundations for intelligent early-warning systems using multi-source remote sensing.

Declaration of generative AI and AI-assisted technologies in the manuscript preparation process

During the preparation of this work, the authors used DeepSeek and ChatGPT in order to improve the language and readability of the manuscript. After using these tools/services, the authors reviewed and edited the content as needed and take full responsibility for the content of the published article.

CRediT authorship contribution statement

Binxiang Qian: Writing – review & editing, Writing – original draft, Validation, Software, Methodology, Formal analysis, Data curation, Conceptualization. **Wenjiang Huang:** Writing – review & editing, Supervision, Funding acquisition, Conceptualization. **Zhijun Zhen:** Writing – review & editing, Supervision. **Kehui Ren:** Formal analysis, Data curation. **Peiqi Yang:** Writing – review & editing, Supervision, Software. **Jianbo Qi:** Writing – review & editing, Supervision, Software. **Michael Henke:** Writing – review & editing, Supervision. **Xiuliang Jin:** Data curation. **Lingjing Ouyang:** Software. **Anting Guo:** Writing – review & editing, Data curation. **Jie Bai:** Writing – review & editing, Supervision. **Chao Ruan:** Writing – review & editing. **Tiecheng Huang:** Writing – review & editing. **Yin Jin:** Writing – review & editing, Writing – original draft, Visualization, Formal analysis. **Zhenong Jin:** Writing – review & editing, Supervision, Funding acquisition, Conceptualization.

Funding

This research was funded by the National Key Research and Development Program of China (Grant No. 2023YFB3906203); the Sino-UK Crop Pest and Disease Forecasting & Management Joint Laboratory (Grant No. 183611ZYLH20240009) supported by MARA; the State Key Program of the National Natural Science Foundation of China (Grant No. 42530109); and the National Natural Science Foundation of China (grant number 42201365).

Declaration of competing interest

The authors declare that they have no known competing financial interests or personal relationships that could have appeared to influence the work reported in this paper.

Acknowledgments

We extend our sincere gratitude to Pablo J. Zarco-Tejada for his invaluable assistance with the FluorSAIL Canopy model, and to Christiaan van der Tol, the architect of the SCOPE model, for the enlightening guidance that has shaped our research direction. Our appreciation also goes to Yelu Zeng and Feng Zhao for their expert guidance on the critical procedures of the mSCOPE model. We are deeply thankful to Huichun Ye, Tianjun Xu, Zhang Yong, Tiange Nie, Senzheng Chen, Peng Wei, Fu Wen, Bohai Hu, Xiangzhe Cheng, Mingxian Zhao, and Xuemei Han for their diligent efforts in gathering field data in Beijing's Tongzhou District. Their contributions have been pivotal to the success of this study. Lastly, we acknowledge the anonymous reviewers for their constructive feedback on the manuscript, which has greatly enhanced the quality of our work.

Appendix A. Supplementary data

Supplementary data to this article can be found online at https://doi.org/10.1016/j.rse.2026.115614.

Data availability

Data will be made available on request.

References

Aloyce, W.M., Kuznetsov, D., Luboobi, L.S., 2017. A mathematical model for the MLND dynamics and sensitivity analysis in a maize population. Asian J. Math. Appl. 2017.

Bai, Y., Jin, X., 2024. Hyperspectral approaches for rapid and spatial plant disease monitoring. Trends Plant Sci. 29, 711–712. https://doi.org/10.1016/j.tplants.2024.03.011.

Bai, Y., Nie, C., Yu, X., Gou, M., Liu, S., Zhu, Y., Jiang, T., Jia, X., Liu, Y., Nan, F., Li, L., Tekinerdogan, B., Song, Y., Liu, Q., Jin, X., 2024. Comprehensive analysis of hyperspectral features for monitoring canopy maize leaf spot disease. Comput. Electron. Agric. 225, 109350. https://doi.org/10.1016/j.compag.2024.109350.

Bai, Y., Zarco-Tejada, P.J., Peñuelas, J., McCabe, M.F., Hawkesford, M.J., Atzberger, C., Poblete, T., Kumar, L., Reynolds, M.P., Nie, C., Song, Y., Yin, D., Zou, D., Liu, S., Liu, Q., Tekinerdogan, B., Jin, X., 2025. Hyperspectral remote sensing for monitoring crop disease: applications, challenges, and perspectives. IEEE Geosci. Remote Sensing Mag. 2-26. https://doi.org/10.1109/MGRS.2025.3603640.

Baret, F., de Solan, B., Lopez-Lozano, R., Ma, K., Weiss, M., 2010. GAI estimates of row crops from downward looking digital photos taken perpendicular to rows at 57.5° zenith angle: theoretical considerations based on 3D architecture models and application to wheat crops. Agric. For. Meteorol. 150, 1393–1401. https://doi.org/10.1016/j.agrformet.2010.04.011.

Cao, X., Luo, Y., Zhou, Y., Duan, X., Cheng, D., 2013. Detection of powdery mildew in two winter wheat cultivars using canopy hyperspectral reflectance. Crop Prot. 45, 124–131. https://doi.org/10.1016/j.cropro.2012.12.002.

Cunniffe, N.J., Stutt, R.O., van den Bosch, F., Gilligan, C.A., 2012. Time-dependent infectivity and flexible latent and infectious periods in compartmental models of plant disease. Phytopathology 102, 365–380. https://doi.org/10.1094/phyto-12-10-0338.

Du, K., Jing, X., Zeng, Y., Ye, Q., Li, B., Huang, J., 2023. An improved approach to monitoring wheat stripe rust with sun-induced chlorophyll fluorescence. Remote Sens. 15, 693.

El Jarroudi, M., Karjoun, H., Hajjami, R., Kouadio, L., El Jarroudi, M., 2025. A spatiotemporal SEIR model for predicting wheat stripe and leaf rusts epidemics. Ecol. Model. 510, 111318. https://doi.org/10.1016/j.ecolmodel.2025.111318.

Féret, J.B., Gitelson, A.A., Noble, S.D., Jacquemoud, S., 2017. PROSPECT-D: towards modeling leaf optical properties through a complete lifecycle. Remote Sens. Environ. 193, 204–215. https://doi.org/10.1016/j.rse.2017.03.004.

Gao, Z., Luo, Z., Zhang, W., Lv, Z., Xu, Y., 2020. Deep learning application in plant stress imaging: a review. AgriEngineering 2, 430–446.

Gastellu-Etchegorry, J.-P., Demarez, V., Pinel, V., Zagolski, F., 1996. Modeling radiative transfer in heterogeneous 3-D vegetation canopies. Remote Sens. Environ. 58, 131–156.

Guo, A., Huang, W., Wang, K., Qian, B., Cheng, X., 2024. Early monitoring of maize northern leaf blight using vegetation indices and plant traits from multiangle hyperspectral data. Agriculture 14, 1311.

Huang, H., Qin, W., Liu, Q., 2013. RAPID: A Radiosity applicable to porous IndiviDual objects for directional reflectance over complex vegetated scenes. Remote Sens. Environ. 132, 221–237. https://doi.org/10.1016/j.rse.2013.01.013.

Jing, X., Li, B., Ye, Q., Zou, Q., Yan, J., Du, K., 2022. Integrate the canopy SIF and its derived structural and physiological components for wheat stripe rust stress monitoring. Remote Sens. 14, 3427.

Kapange, F., Irunde, J.I., Kuznetsov, D., 2019. Modeling transmission dynamics of northern corn leaf blight disease with seasonal weather variations. J. Math. Inform. 15, 33–48. https://doi.org/10.22457/jmi.123av15a4.

Kuusk, A., 2001. A two-layer canopy reflectance model. J. Quant. Spectrosc. Radiat. Transf. 71, 1–9.

Li, X., Huang, H., Shabanov, N.V., Chen, L., Yan, K., Shi, J., 2020. Extending the stochastic radiative transfer theory to simulate BRF over forests with heterogeneous distribution of damaged foliage inside of tree crowns. Remote Sens. Environ. 250, 112040. https://doi.org/10.1016/j.rse.2020.112040.

Li, X., Shabanov, N.V., Chen, L., Zhang, Y., Huang, H., 2022. Modeling solar-induced fluorescence of forest with heterogeneous distribution of damaged foliage by extending the stochastic radiative transfer theory. Remote Sens. Environ. 271, 112892. https://doi.org/10.1016/j.rse.2022.112892.

Liu, L., Song, B., Zhang, S., Liu, X., 2017. A novel principal component analysis method for the reconstruction of leaf reflectance spectra and retrieval of leaf biochemical contents. Remote Sens. 9, 1113.

Liu, S., Jin, X., Feng, H., Nie, C., Bai, Y., Cheng, M., 2023. Analysis of effect of disease stress on maize LAI remote sensing estimation. Trans. Chin. Soc. Agric. Mach. 54, 246–258.

Luo, L., Chang, Q., Wang, Q., Huang, Y., 2021. Identification and severity monitoring of maize dwarf mosaic virus infection based on hyperspectral measurements. Remote Sens. 13, 4560.

Lv, Z., Meng, R., Chen, G., Zhao, F., Xu, B., Zhao, Y., Huang, Z., Zhou, L., Zeng, L., Yan, J., 2023. Combining multiple spectral enhancement features for improving spectroscopic asymptomatic detection and symptomatic severity classification of southern corn leaf blight. Precis. Agric. 24, 1593–1618. https://doi.org/10.1007/s11119-023-10010-2.

Ma, T., Fang, H., 2023. GSV-L: A general spectral vector model for hyperspectral leaf spectra simulation. Int. J. Appl. Earth Obs. Geoinf. 117, 103216. https://doi.org/10.1016/j.jag.2023.103216.

Mahlein, A.-K., 2016. Plant disease detection by imaging sensors – parallels and specific demands for precision agriculture and plant phenotyping. Plant Dis. 100, 241–251. https://doi.org/10.1094/pdis-03-15-0340-fe.

Mahlein, A.K., Rumpf, T., Welke, P., Dehne, H.W., Plümer, L., Steiner, U., Oerke, E.C., 2013. Development of spectral indices for detecting and identifying plant diseases. Remote Sens. Environ. 128, 21–30. https://doi.org/10.1016/j.rse.2012.09.019.

Pfordt, A., Paulus, S., 2024. A review on detection and differentiation of maize diseases and pests by imaging sensors. J. Plant Dis. Protect. 132, 40. https://doi.org/10.1007/s41348-024-01019-4.

Prikaziuk, E., Migliavacca, M., Su, Z., van der Tol, C., 2023. Simulation of ecosystem fluxes with the SCOPE model: sensitivity to parametrization and evaluation with flux tower observations. Remote Sens. Environ. 284, 113324. https://doi.org/10.1016/j.rse.2022.113324.

Qi, J., Xie, D., Guo, D., Yan, G., 2017. A large-scale emulation system for realistic three-dimensional (3-D) forest simulation. IEEE J. Select. Top. Appl. Earth Observ. Remote Sensing 10, 4834–4843.

Qi, J., Xie, D., Yin, T., Yan, G., Gastellu-Etchegorry, J.-P., Li, L., Zhang, W., Mu, X., Norford, L.K., 2019. LESS: LargE-scale remote sensing data and image simulation framework over heterogeneous 3D scenes. Remote Sens. Environ. 221, 695–706. https://doi.org/10.1016/j.rse.2018.11.036.

Qian, B., Huang, W., Jin, Z., Ren, K., Yang, P., Wang, K., Qi, J., Zhen, Z., Henke, M., Bai, J., Jin, Y., Pan, Y., Jiao, Q., Guo, A., Liu, X., 2026. The cmSCOPE Model: A Simple Adaptation of the SCOPE Model to Describe the Vertically Stratified Heterogeneity of Maize Growth and Stress Dynamics (unpublished results) Available at SSRN https://doi.org/10.2139/ssrn.5430238.

Ran, D., Sun, Z., Lu, S., Omasa, K., 2025. An advanced dorsiventral leaf radiative transfer model for simulating multi-angular and spectral reflection: considering asymmetry of leaf internal and surface structure. Remote Sens. Environ. 318, 114531. https://doi.org/10.1016/j.rse.2024.114531.

Savary, S., Willocquet, L., Pethybridge, S.J., Esker, P., McRoberts, N., Nelson, A., 2019. The global burden of pathogens and pests on major food crops. Nat. Ecol. Evol. 3, 430–439. https://doi.org/10.1038/s41559-018-0793-y.

Shabanov, N.V., Knyazikhin, Y., Baret, F., Myneni, R.B., 2000. Stochastic modeling of radiation regime in discontinuous vegetation canopies. Remote Sens. Environ. 74, 125–144.

Shen, Y., Zhao, Y., Chen, G., Lv, Z., Zhao, F., Yang, W., Meng, R., 2024. Identification and severity classification of typical maize foliar diseases based on hyperspectral data. Smart Agric. 6, 28–39. https://doi.org/10.12133/j.smartag.SA202310016.

Song, X., Zhou, G., He, Q., Zhou, H., 2021. Quantitative response of maize Vcmax25 to persistent drought stress at different growth stages. Water 13, 1971.

Soubeyrand, S., Held, L., Höhle, M., Sache, I., 2008. Modelling the spread in space and time of an airborne plant disease. J. R. Stat. Soc.: Ser. C: Appl. Stat. 57, 253–272. https://doi.org/10.1111/j.1467-9876.2007.00612.x.

Tian, L., Xue, B., Wang, Z., Li, D., Yao, X., Cao, Q., Zhu, Y., Cao, W., Cheng, T., 2021. Spectroscopic detection of rice leaf blast infection from asymptomatic to mild stages with integrated machine learning and feature selection. Remote Sens. Environ. 257, 112350. https://doi.org/10.1016/j.rse.2021.112350.

Vilfan, N., van der Tol, C., Muller, O., Rascher, U., Verhoef, W., 2016. Fluspect-B: a model for leaf fluorescence, reflectance and transmittance spectra. Remote Sens. Environ. 186, 596–615. https://doi.org/10.1016/j.rse.2016.09.017.

Wang, Q., Li, P., 2013. Canopy vertical heterogeneity plays a critical role in reflectance simulation. Agric. For. Meteorol. 169, 111–121.

Wang, N., Yang, P., Clevers, J.G.P.W., Wieneke, S., Kooistra, L., 2023. Decoupling physiological and non-physiological responses of sugar beet to water stress from sun-induced chlorophyll fluorescence. Remote Sens. Environ. 286, 113445. https://doi.org/10.1016/j.rse.2022.113445.

Widlowski, J.-L., Mio, C., Disney, M., Adams, J., Andredakis, I., Atzberger, C., Brennan, J., Busetto, L., Chelle, M., Ceccherini, G., Colombo, R., Côté, J.-F., Eenmäe, A., Essery, R., Gastellu-Etchegorry, J.-P., Gobron, N., Grau, E., Haverd, V., Homolová, L., Huang, H., Hunt, L., Kobayashi, H., Koetz, B., Kuusk, A., Kuusk, J., Lang, M., Lewis, P.E., Lovell, J.L., Malenovský, Z., Meroni, M., Morsdorf, F., Mõttus, M., Ni-Meister, W., Pinty, B., Rautiainen, M., Schlerf, M., Somers, B., Stuckens, J., Verstraete, M.M., Yang, W., Zhao, F., Zenone, T., 2015. The fourth phase of the radiative transfer model intercomparison (RAMI) exercise: actual canopy scenarios and conformity testing. Remote Sens. Environ. 169, 418–437. https://doi.org/10.1016/j.rse.2015.08.016.

Xiao, Y., Dong, Y., Huang, W., Liu, L., 2022. Regional prediction of fusarium head blight occurrence in wheat with remote sensing based susceptible-exposed-infectious-removed model. Int. J. Appl. Earth Obs. Geoinf. 114, 103043.

Xu, S., Atherton, J., Riikonen, A., Zhang, C., Oivukkamäki, J., MacArthur, A., Honkavaara, E., Hakala, T., Koivumäki, N., Liu, Z., Porcar-Castell, A., 2021. Structural and photosynthetic dynamics mediate the response of SIF to water stress in a potato crop. Remote Sens. Environ. 263, 112555. https://doi.org/10.1016/j.rse.2021.112555.

Xue, B., Kong, Y., Zarco-Tejada, P., Tian, L., Poblete, T., Wang, X., Zheng, H., Jiang, C., Yao, X., Zhu, Y., Cao, W., Cheng, T., 2026. Mitigating the phenological influence on spectroscopic quantification of rice blast disease severity with extended PROSAIL simulations. Remote Sens. Environ. 332, 115063. https://doi.org/10.1016/j.rse.2025.115063.

Yang, P., Verhoef, W., van der Tol, C., 2017. The mSCOPE model: A simple adaptation to the SCOPE model to describe reflectance, fluorescence and photosynthesis of vertically heterogeneous canopies. Remote Sens. Environ. 201, 1–11.

Yang, P., Prikaziuk, E., Verhoef, W., van Der Tol, C., 2021. SCOPE 2.0: A model to simulate vegetated land surface fluxes and satellite signals. Geosci. Model Dev. 14, 4697–4712.

Zeng, Y., Chen, M., Hao, D., Damm, A., Badgley, G., Rascher, U., Johnson, J.E., Dechant, B., Siegmann, B., Ryu, Y., Qiu, H., Krieger, V., Panigada, C., Celesti, M., Miglietta, F., Yang, X., Berry, J.A., 2022. Combining near-infrared radiance of vegetation and fluorescence spectroscopy to detect effects of abiotic changes and stresses. Remote Sens. Environ. 270, 112856. https://doi.org/10.1016/j.rse.2021.112856.

Zhang, J., Pu, R., Huang, W., Yuan, L., Luo, J., Wang, J., 2012. Using in-situ hyperspectral data for detecting and discriminating yellow rust disease from nutrient stresses. Field Crop Res. 134, 165–174. https://doi.org/10.1016/j.fcr.2012.05.011.

Zhang, J., Huang, Y., Pu, R., Gonzalez-Moreno, P., Yuan, L., Wu, K., Huang, W., 2019. Monitoring plant diseases and pests through remote sensing technology: a review. Comput. Electron. Agric. 165, 104943. https://doi.org/10.1016/j.compag.2019.104943.

Zhang, W., Yang, G., Qi, J., Chen, R., Zhang, C., Xu, B., Wu, B., Su, X., Zhao, C., 2025. The impacts of tree shape, disease distribution and observation geometry on the performances of disease spectral indices of apple trees. Remote Sens. Environ. 329, 114953. https://doi.org/10.1016/j.rse.2025.114953.

Zhao, X., Qi, J., Xu, H., Yu, Z., Yuan, L., Chen, Y., Huang, H., 2023. Evaluating the potential of airborne hyperspectral LiDAR for assessing forest insects and diseases with 3D radiative transfer Modeling. Remote Sens. Environ. 297, 113759. https://doi.org/10.1016/j.rse.2023.113759.